Fractional quantum Hall physics and higher-order momentum correlations in a few spinful fermionic contact-interacting ultracold atoms in rotating traps

Constantine Yannouleas* and Uzi Landman†
School of Physics, Georgia Institute of Technology, Atlanta, Georgia 30332-0430, USA

(Received 14 June 2020; accepted 14 September 2020; published 16 October 2020)

The fractional quantum Hall effect (FQHE) is theoretically investigated, with numerical and algebraic approaches, in assemblies of a few spinful ultracold neutral fermionic atoms, interacting via repulsive contact potentials and confined in a single rapidly rotating two-dimensional harmonic trap. Going beyond the commonly used second-order correlations in the real configuration space, the methodology in this paper will assist the analysis of experimental observations by providing benchmark results for N-body spin-unresolved, as well as spin-resolved, momentum correlations measurable in time-of-flight experiments with individual particle detection. Our analysis shows that the few-body lowest-Landau-level (LLL) states with good magic angular momenta exhibit inherent ordered quantum structures in the N-body correlations, similar to those associated with rotating Wigner molecules (WMs), familiar from the field of semiconductor quantum dots under high magnetic fields. The application of a small perturbing stirring potential induces, at the ensuing avoided crossings, formation of symmetry-broken states exhibiting ordered polygonal-ring structures, explicitly manifest in the single-particle density profile of the trapped particles. Away from the crossings, an LLL state obtained from exact diagonalization of the microscopic Hamiltonian, found to be well described by a (1,1,1) Halperin two-component variational wave function, represents also a spinful rotating WM. Analysis of the calculated LLL wave function enables a two-dimensional generalization of the Girardeau one-dimensional "fermionization" scheme, originally invoked for mapping of bosonic-type wave functions to those of spinless fermions.

DOI: 10.1103/PhysRevA.102.043317

I. INTRODUCTION

The discovery [1] of the fractional quantum Hall effect (FQHE) in extended (bulk) electronic semiconductor samples of high purity, cooled down to low temperatures, and subjected to high perpendicular magnetic fields gave rise to a new subfield in condensed-matter physics, resulting in a large number of both experimental and theoretical investigations of correlated states of interacting electronic systems exhibiting emergent topological phases of matter. Among the theoretical approaches, we note in particular those based on the introduction of families of variational wave functions in the lowest Landau level (LLL) (see, e.g., Refs. [2–6]), following Laughlin's seminal publications [2,3].

The unprecedented experimental advances achieved recently in the area of trapped ultracold neutral atoms generated intense interest in finite-size bosonic analogs [7–14] of the FQHE, being embodied in clouds of a few ultracold atoms trapped in rotating harmonic traps, with the rotation acting as a synthetic (rotational gauge) magnetic field.

The expansion of the horizon of such LLL investigations to encompass the regime of a few ultracold spinful fermionic atoms is a natural undertaking. Theoretical investigations of such an endeavor, presented in this paper, are further supported by a growing number of recent experimental advances [15–19] in the deterministic control of assemblies of a few (N) trapped ^{6}Li atoms, and in particular by the anticipated implementation [20] of a single rapidly rotating two-dimensional (2D) harmonic trap able to project the few-body wave functions within the LLL Hilbert space.

We use state-of-the-art computational tools based on exact diagonalization of the microscopic Hamiltonian with the use of the full configuration interaction (CI) methodology, as was adapted to two dimensions [21–25], in contrast to the familiar three-dimensional (3D) CI chemistry formalism [26]; indeed, this approach has been proved successful in previous studies of few bosons [11] or electrons [21,27] in the LLL. Our study will assist the analysis of experimental observations by providing benchmark results for N-body (spin-unresolved, as well as spin-resolved) momentum correlations that can be measured directly with time-of-flight (TOF) protocols employing individual particle detection through fluorescent imaging in free space [17–19,28]. Such research endeavors aim at revealing the microscopic structure of the correlated FQHE states (here for contact-interacting spinful fermions), adding, supplementing, and going beyond the information gained from studies of bulk properties, e.g., Hall resistance. In this respect, the approach in this paper, demonstrated earlier for a few bosons in Ref. [11], goes beyond the common theoretical analyses that are based on second-order correlations in the real configuration space [3,10,21].

The main issues discussed and analyzed in this work include the following:

*Constantine.Yannouleas@physics.gatech.edu
†Uzi.Landman@physics.gatech.edu

(1) The formation of few-body LLL states with magic angular momenta [29–31] exhibiting intrinsic ordered structures in the N-body correlations. Such ordered quantum structures, referred to commonly as rotating Wigner molecules (RWMs) [21,31,32], have been seen previously in the case of semiconductor quantum dots (electrons) under high magnetic fields. Here they are shown to appear even in the case of ultracold contact interacting fermionic atoms confined in a rotating trap.

(2) The application of a small perturbing stirring potential V_P to the rotating trap, as described in experimental protocols [9,13,14], where this perturbation enables transition between good-total-L states. In the presence of V_P, symmetry-broken states (referred to as pinned Wigner molecules [27,33]) emerge in the neighborhood of ensuing avoided crossings, exhibiting the ordered structures already at the lowest level of the first-order correlations, i.e., the single-particle densities.

(3) A CI-calculated LLL state, corresponding to Halperin's (1,1,1) variational wave function [4], is shown to provide an example of both a rotating Wigner molecule and of a generalization to two dimensions of Girardeau's one-dimensional "fermionization" scheme [16,34], originally invoked for designating the mapping of bosonic-type wave functions to those of spinless fermions.

The above theoretical predictions can be explicitly tested through analysis of experimentally determined momentum correlations, that is, including up to Nth-order correlation functions obtained for N fermionic atoms confined in the rotating trap via time-of-flight measurements.

Plan of paper

The plan of the paper is given below. Following this Introduction section, we present in Sec. II theoretical preliminaries which aim at defining the problem, establishing notations, and giving a brief survey of the methodologies and techniques employed in this study. In more detail: Section II A presents the microscopic many-body Hamiltonian of ultracold fermionic atoms (here four ^{6}Li) confined in a rapidly rotating (stirred up) trap, with or without a perturbation V_P, that breaks the cylindrical symmetry of the trap. Section II B describes the configuration interaction method used to obtain numerical solutions of the Hamiltonian via exact diagonalization of the microscopic Hamiltonian, with illustrations of the effect of the perturbation, resulting in avoided crossings, depending on the strength of V_P, between neighboring eigenstates of the unperturbed Hamiltonian; in most calculations demonstrated in this paper, we consider a V_P perturbing stirring potential of hexadecapolar symmetry in the many-body Hamiltonian.

Section II C discusses the tools of analysis used in this investigation, in particular, the spin-unresolved and spin-resolved correlation functions, that is, single-particle, first-order, correlation function (i.e., CI-single-particle density), and higher-order (up to fourth-order) correlation functions in real coordinate space. Section II D describes these tools of analysis in the momentum space, that is, it discusses the Fourier transforms of the real-space correlation functions, as measured in TOF measurements of particles propagating in free space after confinement removal.

In Sec. III, we discuss the LLL spectra and the concept of magic angular momenta, including the combined effects of the rotational and spin degrees of freedom; a group theoretical discussion of the geometrical-symmetry origins of the magic angular momenta sequences can be found in Appendix A. Section IV is devoted to analysis of the properties of the ground state in the spin sector ($S = 0,\ S_z = 0$) of the four ^{6}Li trapped and rotating atoms while traversing an avoided crossing, originating from the symmetry-breaking perturbation V_P. This includes illustration of the formation of a pinned crystalline-ordered (square) symmetry-broken single-particle density, revealed in the single-particle density three-dimensional surface plots; see Sec. IV A. Away from the avoided crossing, the circular symmetry of the single-particle density is automatically reestablished, and the crystalline order becomes intrinsic and hidden, but it can still be revealed in the Nth-order (here fourth-order) correlation function (Sec. IV B). Second-order correlations are discussed in Sec. IV C, and the spin structure of the ground state is analyzed in Sec. IV D. These results illustrate the formation of a quantum ultracold rotating-Wigner molecule (UC-RWM) of square symmetry, and have been obtained for the case of a hexadecapolar stirring potential. In Sec. IV E, we illustrate the formation of an UC-RWM for the case of $N = 4$ for a quadrupolar trap deformation. The resulting molecule is shown to be closely similar to the one obtained for the hexadecapolar perturbation, even though the symmetry of the quadrupolar stirring potential does not coincide with the square symmetry.

One of the main foci of this work is addressed in Sec. V, namely, examination of the generalization of the Laughlin wave function by Halperin to include FQHE spinful (non-spin-polarized) configurations. To this end, we concentrate our discussion on the spin sector ($S = 2,\ S_z = 0$) of the four ^{6}Li ultracold atoms in the rotating trap, and compare the predictions of our exact-diagonalization CI calculations for the structure of the ground state in this sector with that of the Halperin (1,1,1) trial function. The presentation in Sec. V includes three subsections: Sec. V A: the fourth-order correlation and the molecular configuration predicted for the ground state of above spin sector by the CI calculation; Sec. V B: comparison between CI state and trial (1,1,1) Halperin wave function; Sec. V C: examination of the limitations of analysis of the CI wave function in the ($S = 2,\ S_z = 0$) spin sector when using second-order correlations [particularly for angular momenta corresponding to the (1,1,1) Halperin state], showing the advantages offered by the N-body correlation function (here $N = 4$).

In Sec. VI, we discuss and illustrate a fermionization analogy in two dimensions, enabled by derivation of appropriate analytic expressions for the calculated exact CI wave function. This is done for the angular momentum $L = 6$ for $N = 4$ fermions in Sec. VI A, and for $L = 15$ for $N = 6$ fermions in Sec. VI B

In Sec. VII, we pause to discuss a comparison between the Wigner parameter R_W, specifying the interparticle interaction strength, and used to define the regime of formation of crystal-like-ordered geometric configurations (that is, quantum Wigner-molecule formations) for confined particles interacting via sufficiently long-range interactions (such as Coulomb-interacting electrons in quantum dots, or the forces between trapped atoms interacting via dipolar interaction

potentials), and the parameter R_δ used as the strength of short-range contact interactions between trapped neutral ultracold atoms in fastly rotating traps (that is, in the LLL regime). We summarize in Sec. VIII.

II. THEORETICAL PRELIMINARIES

A. Many-body Hamiltonian

The Fock-Darwin spectrum [35,36] associated with the (n, l) single-particle states in a rapidly rotating two-dimensional (2D) trap is given by [37]

$$\epsilon_{n,l}^{\mathrm{FD}} = \hbar[(2n + |l| + 1)\omega - l\Omega], \tag{1}$$

where ω is the trapping frequency of the harmonic confinement, Ω is the rotational frequency of the trap, n is the number of nodes, and l denotes the single-particle angular momentum. The projection on the LLL imposes $n = 0$ (Fock-Darwin single-particle states without radial nodes), and the associated many-body Hamiltonian without the perturbing contribution is [38]

$$\frac{H_{\mathrm{LLL}}}{\hbar\omega} = N + \left(1 - \frac{\Omega}{\omega}\right)L + 2\pi R_\delta \sum_{i<j}^{N} \delta(\mathbf{r}_i - \mathbf{r}_j), \tag{2}$$

where N is the number of particles, and L denotes the total angular momentum, $L = \sum_{i=1}^{N} l_i$, along the axis perpendicular to the 2D trap plane. The energies in Eq. (2) are in units of $\hbar\omega$ and the lengths in units of the oscillator length $\Lambda = \sqrt{\hbar/(M\omega)}$. Here, the first and second terms express the LLL kinetic-energy contribution H_K, whereas the third term represents the contact-interaction contribution H_{int}.

The dimensionless parameter

$$R_\delta = \frac{g}{2\pi\Lambda^2\hbar\omega} = \frac{gM}{2\pi\hbar^2} \tag{3}$$

expresses the strength g of the coupling constant associated with an area $2\pi\Lambda^2$, relative to the zero-point energy $\hbar\omega$ associated with the 2D harmonic trap; M is the mass of the ultracold fermionic atoms. Naturally, the δ functions in Eq. (2) are two dimensional.

For the quasi-2D traps realized in experiments, the coupling constant g, as a function of the 3D scattering length a_s and the oscillator length $l_z = \sqrt{\hbar/(M\omega_z)}$ in the tight transverse direction, can be calculated numerically by considering the s channel in a two-particle scattering problem [39]. When a_s is smaller than l_z, the analytic expression $R_\delta = \sqrt{2/\pi}\,a_s/l_z$ [40], can also be derived using the expression for the coupling constant in Eq. (11) of Ref. [39]; see also Eq. (1.122) in Ref. [41]. Experimentally, the 3D scattering length can be varied over a wide range with the use of the Feshbach resonance; e.g., for ^{6}Li atoms, see Refs. [42,43]. We note that the organization of the LLL trapped atoms in geometric structures of particular symmetries (that is, the formation of LLL ultracold-atom Wigner molecules, discussed below) is independent of the precise value of R_δ; for further discussion, see Sec. VII.

Another way for interpreting the parameter R_δ is that it equals the direct matrix element [see Eqs. (11), (13), and (14) below]

$$e_{\max} = \langle l_1 = 0, l_2 = 0|H_{\mathrm{int}}|l_3 = 0, l_4 = 0\rangle = R_\delta. \tag{4}$$

$e_{\max}$ is in units of $\hbar\omega$ and the subscript "max" indicates that this energy represents the maximum repulsion that two fermions with opposite spins can attain in the LLL Hilbert space. Since the energy gap between the lowest and the first-excited Landau levels is $2\hbar\omega$ (see the Appendix in Ref. [31]), the condition for validating the projection of the few-body problem in the LLL is $R_\delta < 2$. In the following, for all calculations, we use a value of $R_\delta = 0.4$ [44].

Adding a small perturbation V_P, the total many-body Hamiltonian becomes

$$H_{\mathrm{MB}} = H_{\mathrm{LLL}} + V_P. \tag{5}$$

Traditionally, a V_P perturbation or its effects have not been considered in the literature of the electronic FQHE (see, e.g., Refs. [2–6]), with the exceptions of Refs. [27] and [33] in the context of disorder effects in the semiconductor sample and on the edge states in graphene quantum dots, respectively. A tunable V_P perturbation representing a multipole deformation of the shape of the rotating harmonic trap [see Eq. (6) below] has been proposed in Refs. [9,13] as the building block of protocols for experimentally controlled assemblies of a few ultracold bosonic atoms enabling simulations of states characterized by well-known trial FQHE states, like the bosonic Laughlin ones. A proposal to use this type of perturbation in order to simulate well-known variational spinful FQHE states with ultracold ^{6}Li atoms has been advanced in Ref. [20]. To this effect, consideration of energy spectra and spatial correlations up to second order was sufficient. By considering higher-order correlations (both spatial and momentum ones) beyond the second order, and investigating the spontaneous symmetry breaking induced by the V_P perturbation in the regions of the avoided crossings, we focus here on previously unexplored fundamental properties of the many-body LLL states of a finite-size assembly of spinful, contact-interacting ultracold atoms.

For reasons of experimental convenience in transitioning from one LLL state to another, it has been shown [9,13,20] that the following perturbation (in second quantization), associated with a small multipole deformation of the rotating trap, is desirable:

$$\frac{V_P}{\hbar\omega} = \mathcal{C}\left(\sum_l \frac{\sqrt{(l+m)!}}{2^{m/2}\sqrt{l!}} a_{l+m}^\dagger a_l + \mathrm{H.c.}\right), \tag{6}$$

where m is the order of the multipole deformation, and $\mathcal{C}$ is a dimensionless constant specifying the strength of the deformation. This perturbation can be introduced as a stirring potential. It couples the many-body solutions of H_{LLL} that differ by m units in their total angular momenta L, and generates avoiding crossings, with an example given in Fig. 1. Note that in showing the spectra of H_{MB}, we limit ourselves to a particular spin sector; in Fig. 1 for $N = 4$, the spin sector is $(S = 0,\ S_z = 0)$, with the lowest-in-energy state within the spin sector termed "the relative ground state."

For a small value of the parameter $\mathcal{C}$ (e.g., $\mathcal{C} = 0.0001$), V_P couples mainly the two originally (when $V_P = 0$) crossing states with good total L and $L + m$, or $L - m$ and L. In this

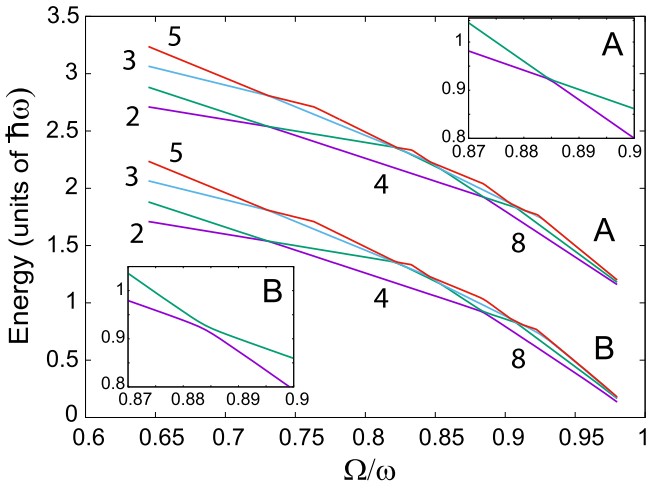

FIG. 1. Spectra of the four lowest-in-energy CI solutions of the many-body Hamiltonian $H_{\rm MB}$ [Eq. (5)] for $N = 4$ fermions as a function of the ratio Ω/ω (the constant energy $N\hbar\omega$ has been subtracted). The spin sector with ($S = 0$, $S_z = 0$) is displayed. $R_\delta = 0.4$ and $m = 4$ (hexadecapole trap deformation). Label A corresponds to $\mathcal{C} = 0.0001$ (weak V_P perturbation). Label B corresponds to $\mathcal{C} = 0.004$ (strong V_P perturbation). The energies associated with label A have been shifted upward by $1\hbar\omega$. The integers next to the curves denote the corresponding ideal good total angular momenta in the absence of any perturbation ($V_P = 0$). In the relative ground state (lowest-in-energy state within the spin sector), only the magic angular momenta 2, 4, and 8 appear (see Sec. III). The nonzero value of $\mathcal{C} = 0.004$ generates a visible (stronger) avoided crossing in the neighborhood of $\Omega/\omega \sim 0.884$, which is magnified in the inset labeled B. For the much smaller value of $\mathcal{C} = 0.0001$, this avoided crossing is minute, as seen from the inset labeled A (no energy shift). Overall, with the naked eye, the two spectra A and B are difficult to differentiate. However, the effect of a weak versus strong perturbation is pronounced on the properties (correlations) of the many-body wave functions when traversing the avoided crossing, as it is discussed in Sec. IV A.

case, the expectation value $\langle L\rangle$ of the total angular momentum along the avoided crossing exhibits a sharp stepwise profile; see Fig. 2(a). A larger value of the parameter $\mathcal{C}$ introduces additional couplings to $L \pm 2m$, $L \pm 3m$, etc., states, which may become non-negligible, and simultaneously the $\langle L\rangle$ profile along the avoided crossing broadens and exhibits a slower variation rate; see Fig. 2(b) for the strong-coupling case of $\mathcal{C} = 0.004$.

B. Configuration interaction method

Denoting the spin degree of freedom by σ, in the CI method, one writes the many-body wave function $\Phi_{\rm CI}(\mathbf{r}_1\sigma_1, \mathbf{r}_2\sigma_2, \ldots, \mathbf{r}_N\sigma_N)$ as a linear superposition of Slater determinants $\Psi(\mathbf{r}_1\sigma_1, \mathbf{r}_2\sigma_2, \ldots, \mathbf{r}_N\sigma_N)$ that span the many-body Hilbert space and are constructed out of the single-particle *spin orbitals*

$$\chi_j(\mathbf{r}) = \psi_j(\mathbf{r})\alpha \quad \text{if} \quad 1 \leqslant j \leqslant K \tag{7}$$

and

$$\chi_j(\mathbf{r}) = \psi_{j-K}(\mathbf{r})\beta \quad \text{if} \quad K < j \leqslant 2K, \tag{8}$$

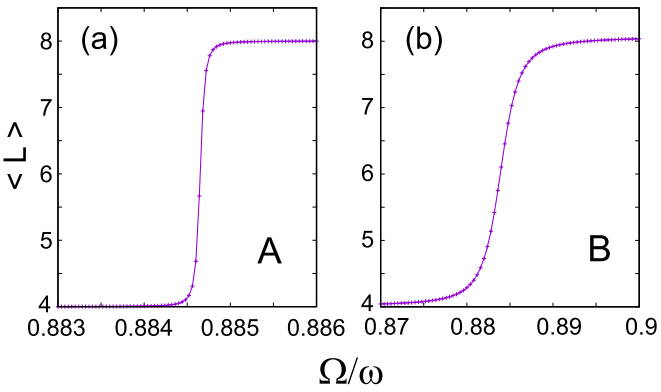

FIG. 2. Expectation values of the total angular momentum $\langle L\rangle$ for $N = 4$ fermions and for the relative ground state in the spin sector ($S = 0$, $S_z = 0$). (a) $\mathcal{C} = 0.0001$ corresponding to the avoided crossing highlighted in the inset labeled as A in Fig. 1. (b) $\mathcal{C} = 0.004$ corresponding to the avoided crossing highlighted in the inset labeled as B in Fig. 1. Note the pronounced difference between (a) and (b) in the displayed ranges of trap rotational frequencies (horizontal axes). $m = 4$ and $R_\delta = 0.4$.

where α (β) denotes up (down) spins. Namely, the wave function of the qth CI state is given by

$$\Phi^q_{\rm CI}(\mathbf{r}_1\sigma_1, \ldots, \mathbf{r}_N\sigma_N) = \sum_I c^q(I)\Psi_I(\mathbf{r}_1\sigma_1, \ldots, \mathbf{r}_N\sigma_N), \tag{9}$$

where

$$\Psi_I = \frac{1}{\sqrt{N!}}\begin{vmatrix} \chi_{j_1}(\mathbf{r}_1) & \cdots & \chi_{j_N}(\mathbf{r}_1) \\ \vdots & \ddots & \vdots \\ \chi_{j_1}(\mathbf{r}_N) & \cdots & \chi_{j_N}(\mathbf{r}_N) \end{vmatrix}, \tag{10}$$

and the master index I counts the number of arrangements $\{j_1, j_2, \ldots, j_N\}$ under the restriction that $1 \leqslant j_1 < j_2 < \cdots < j_N \leqslant 2K$. Of course, $q = 1, 2, \ldots$ counts the excitation spectrum, with $q = 1$ corresponding to the overall ground state for each total spin projection S_z.

Because we restrict the Hilbert space in the LLL, the single-particle spatial orbitals are nodeless and they are given in polar coordinates by the expression

$$\psi_l(\mathbf{r}) = \frac{1}{\sqrt{\pi\, l!}} r^l e^{il\theta} e^{-r^2/2}, \tag{11}$$

where $l \geqslant 0$ is the single-fermion angular momentum, and r is in units of the oscillator length $\Lambda = \sqrt{\hbar/(M\omega)}$.

Next, the CI (exact) diagonalization of the many-body Schrödinger equation

$$H_{\rm MB}\Phi^q_{\rm CI} = E^q_{\rm CI}\Phi^q_{\rm CI} \tag{12}$$

transforms into a matrix diagonalizatiom problem, which yields the coefficients $c^q(I)$ and the CI eigenenergies $E^q_{\rm CI}$. Because the resulting matrix is sparse, we implement its numerical diagonalization employing the very efficient ARPACK solver [45] of large-scale eigenvalue problems with implicitly restarted Arnoldi methods [46].

The matrix elements $\langle\Psi_I|H_{\rm MB}|\Psi_J\rangle$ between the basis determinants [see Eq. (10)] are calculated using the Slater rules [26]. Naturally, important ingredients in this respect are the

two-body matrix elements of the contact interaction

$$V_{1234} = \int_{-\infty}^{\infty}\int_{-\infty}^{\infty} d\mathbf{r}_i d\mathbf{r}_j \psi_1^*(\mathbf{r}_i)\psi_2^*(\mathbf{r}_j)\delta(\mathbf{r}_i-\mathbf{r}_j) \times \psi_3(\mathbf{r}_i)\psi_4(\mathbf{r}_j), \tag{13}$$

in the basis formed out of the single-particle spatial orbitals $\psi_i(\mathbf{r})$, $i = 1, 2, \ldots, K$ [Eq. (11)]. When the lengths are expressed in units of Λ, these matrix elements are dimensionless and are given analytically by [47]

$$V_{1234} = \frac{1}{2\pi}\frac{\delta_{l_1+l_2,l_3+l_4}}{\sqrt{l_1!l_2!l_3!l_4!}}\frac{(l_1+l_2)!}{2^{l_1+l_2}}. \tag{14}$$

The Slater determinants Ψ_I [see Eq. (10)] conserve the third projection S_z, but not the square $\hat{\mathbf{S}}^2$ of the total spin. However, because $\hat{\mathbf{S}}^2$ commutes with the many-body Hamiltonian, the nondegenerate CI solutions are automatically eigenstates of $\hat{\mathbf{S}}^2$ with eigenvalues $S(S+1)$. After the diagonalization, these eigenvalues are determined by applying $\hat{\mathbf{S}}^2$ onto $\Phi_{\rm CI}^q$ and using the relation

$$\hat{\mathbf{S}}^2\Psi_I = \left[(N_\uparrow - N_\downarrow)^2/4 + N/2 + \sum_{i<j}\varpi_{ij}\right]\Psi_I, \tag{15}$$

where the operator ϖ_{ij} interchanges the spins of fermions i and j provided that their spins are different; $N_\uparrow$ and $N_\downarrow$ denote the number of spin-up and spin-down fermions, respectively.

C. Tools of analysis: Real configuration space

The tools of analysis used in this paper are the single-particle densities (first-order correlations), the spin-*un*resolved and spin-resolved second-order correlations, as well as the higher-order N-body correlations (fourth order for $N = 4$ fermions).

The spin-unresolved CI single-particle densities (first-order correlation functions) are given by

$$\rho_{\rm CI}(\mathbf{r}) =^1 \mathcal{G}(\mathbf{r}) = \langle\Phi_{\rm CI}|\sum_{i=1}^{N}\delta(\mathbf{r}_i-\mathbf{r})|\Phi_{\rm CI}\rangle. \tag{16}$$

Here and in the following, it is understood that evaluation of expectation values over the many-body wave function $\Phi_{\rm CI}(\mathbf{r}_1\sigma_1, \ldots, \mathbf{r}_N\sigma_N)$ involves integration over all the particles' coordinates (including the spin ones).

We note that, in the case of a single Slater determinant, the above definition yields the simple formula of summation over the modulus square of the single-particle spatial orbitals. The spin-unresolved second-order correlations (pair correlations) are specified as

$${}^2\mathcal{G}(\mathbf{r},\mathbf{r}_0) = \langle\Phi_{\rm CI}|\sum_{i\neq j}\delta(\mathbf{r}-\mathbf{r}_i)\delta(\mathbf{r}_0-\mathbf{r}_j)|\Phi_{\rm CI}\rangle, \tag{17}$$

whereas the definition of the spin-resolved second-order correlations (pair correlations) includes the spin degree of freedom as follows:

$${}^2\mathcal{G}_{\sigma\sigma_0}(\mathbf{r},\mathbf{r}_0) = \langle\Phi_{\rm CI}|\sum_{i\neq j}\delta(\mathbf{r}-\mathbf{r}_i)\delta(\mathbf{r}_0-\mathbf{r}_j)\delta_{\sigma\sigma_i}\delta_{\sigma_0\sigma_j}|\Phi_{\rm CI}\rangle. \tag{18}$$

The spin-resolved ${}^2\mathcal{G}_{\sigma,\sigma_0}$ is also referred to as conditional probability distribution (CPD) [27,31] because it gives the spatial probability distribution for finding a second fermion with spin projection σ under the condition that a first fermion with spin projection σ_0 is fixed at $\mathbf{r}_0$; σ and σ_0 can be either up ($\uparrow$) or down ($\downarrow$). The first- and second-order correlations defined above are calculated using the Slater rules [48] for the matrix elements between determinants of one- and two-body operators, respectively.

More importantly, here, we use in addition higher-order correlations, and in particular the N-body correlations (fourth order for $N = 4$ fermions which are the focus of this paper). To motivate our discussion, we start first with the case of four fully polarized fermions ($S = 2$ and $S_z = 2$), whose spatial part is equivalent to the case of spinless fermions. For this case the CI wave function can be written as

$$\Phi_{\rm CI}(\mathbf{r}_1\alpha(1),\mathbf{r}_2\alpha(2),\mathbf{r}_3\alpha(3),\mathbf{r}_4\alpha(4)) = F(\mathbf{r}_1,\mathbf{r}_2,\mathbf{r}_3,\mathbf{r}_4)\alpha(1)\alpha(2)\alpha(3)\alpha(4), \tag{19}$$

and the fourth-order correlation function is given simply by the modulus square of the spatial part, i.e.,

$${}^4\mathcal{G}_{\rm CI}(\mathbf{r}_1,\mathbf{r}_2,\mathbf{r}_3,\mathbf{r}_4) = |F(\mathbf{r}_1,\mathbf{r}_2,\mathbf{r}_3,\mathbf{r}_4)|^2. \tag{20}$$

The cases of non-spin-polarized configurations are more complicated, involving both spin-resolved and spin-unresolved correlations. In general, in the case of N spinful fermions (with $N = N_\uparrow + N_\downarrow$), the CI wave function $\Phi_{\rm CI}$ contains $K = N!/(N_\uparrow N_\downarrow)$ primitive spin functions of the form

$$\zeta_i(N_\uparrow, N_\downarrow) = \alpha\alpha\ldots\beta\beta. \tag{21}$$

To be specific, for the case of $N = 4$ fermions with $N_\uparrow = N_\downarrow = 2$ ($S_z = 0$), there are $K = 6$ such spin primitives, namely,

$$\begin{aligned}
\zeta_1 &= \alpha(1)\alpha(2)\beta(3)\beta(4),\\
\zeta_2 &= \alpha(1)\alpha(3)\beta(2)\beta(4),\\
\zeta_3 &= \alpha(1)\alpha(4)\beta(2)\beta(3),\\
\zeta_4 &= \alpha(2)\alpha(3)\beta(1)\beta(4),\\
\zeta_5 &= \alpha(2)\alpha(4)\beta(1)\beta(3),\\
\zeta_6 &= \alpha(3)\alpha(4)\beta(1)\beta(2),
\end{aligned} \tag{22}$$

where the arguments from 1 to 4 in the α's and β's correspond to particle indices.

Considering the four spin orbitals $u_1^I = \phi_{l_1}^I\alpha$, $u_2^I = \phi_{l_2}^I\alpha$, $u_3^I = \phi_{l_3}^I\beta$, and $u_4^I = \phi_{l_4}^I\beta$ of the Ith determinant in the CI expansion [Eq. (9)], which (for a given determinant) are the same for all six ζ's listed in Eq. (22), the many-body CI wave function for $N_\uparrow = N_\downarrow = 2$ can be rewritten as

$$\Phi_{\rm CI} = \sum_{i=1}^{6}\mathcal{F}_i(\mathbf{r}_1,\mathbf{r}_2,\mathbf{r}_3,\mathbf{r}_4)\zeta_i, \tag{23}$$

where

$$\mathcal{F}_i = \sum_I c(I)\mathrm{Det}^\uparrow\left[\phi_{l_1}^I(\mathbf{s}_1^i),\phi_{l_2}^I(\mathbf{s}_2^i)\right]\mathrm{Det}^\downarrow\left[\phi_{l_3}^I(\mathbf{s}_3^i),\phi_{l_4}^I(\mathbf{s}_4^i)\right], \tag{24}$$

where $c(I)$ are the coefficients of the CI expansion and $(\mathbf{s}_1^i, \mathbf{s}_2^i)$ and $(\mathbf{s}_3^i, \mathbf{s}_4^i)$ coincide with the spatial coordinates associated with the particle indices for the up and down spins in the ζ_i spin primitives defined in Eq. (22). For example, for $i = 5$, one has

$$\begin{aligned} \mathbf{s}_1^5 &\rightarrow \mathbf{r}_2, \\ \mathbf{s}_2^5 &\rightarrow \mathbf{r}_4, \\ \mathbf{s}_3^5 &\rightarrow \mathbf{r}_1, \\ \mathbf{s}_4^5 &\rightarrow \mathbf{r}_3. \end{aligned} \tag{25}$$

The spin-unresolved fourth-order correlation is then given by

$$^4\mathcal{G}_{\rm CI}^{\rm un} = \sum_{i=1}^{6} \mathcal{F}_i^* \mathcal{F}_i. \tag{26}$$

The spin resolved fourth-order correlations are defined as a partial summation over the spin-primitive index i [Eq. (22)]. For example, the probability of finding the fourth fermion with spin down [$\beta(4)$ in any ζ_i spin primitive] at a position $\mathbf{r}$, given the positions of the first three fermions with unresolved spins, is

$$^4\mathcal{G}_{\rm CI}^{\rm res,1} = \mathcal{F}_1^* \mathcal{F}_1 + \mathcal{F}_2^* \mathcal{F}_2 + \mathcal{F}_4^* \mathcal{F}_4. \tag{27}$$

Other spin-resolved fourth-order correlations are possible: for example, finding the fourth fermion with spin down at position $\mathbf{r}$, given the positions of the first three fermions with the second fermion having a spin up and the first and third ones with unresolved spins is given by

$$^4\mathcal{G}_{\rm CI}^{\rm res,2} = \mathcal{F}_1^* \mathcal{F}_1 + \mathcal{F}_4^* \mathcal{F}_4. \tag{28}$$

D. Tools of analysis: Momentum space

To channel our discussion about momentum-space correlation functions, we recall again that, usually, a CI calculation (or other exact-diagonalization schemes used for solution of the microscopic many-body Hamiltonian) yields a many-body wave function (e.g., $\Phi_{\rm CI}$) in position coordinates $(\mathbf{r}_1\sigma_1, \mathbf{r}_2\sigma_2, \ldots, \mathbf{r}_N\sigma_N)$; see Eq. (9), which for the case of $N = 4$ fermions can take the form in Eq. (23).

The CI wave functions $\Phi_{\rm CI}$ are particularly conducive for carrying out their mapping into the momentum-space ones $\Phi_{\rm CI}^{\mathcal{M}}$; naturally, the momentum space is spanned by the coordinates $(\mathbf{k}_1\sigma_1, \mathbf{k}_2\sigma_2, \ldots, \mathbf{k}_N\sigma_N)$, with $\mathbf{k}_j = \mathbf{p}_j/\hbar$. Indeed, it is sufficient to replace each LLL single-particle real-space orbital $\psi_j(\mathbf{r})$ in the basis determinants Ψ_I [Eq. (10)] by its 2D Fourier transform, which is given by [compare to the real-space function in Eq. (11)]

$$\psi_l(\mathbf{k}) = \frac{i^l}{\sqrt{\pi l!}} k^l e^{il\varphi} e^{-k^2/2}, \tag{29}$$

where k is in units of the inverse of the oscillator length $1/\Lambda$; see definition after Eq. (11).

Having obtained the many-body wave function in real space, all and each formula (in Sec. II C) specifying the tools of analysis in real space (first-, second-, and Nth-order correlations) can be immediately translated in momentum space by simply replacing $\mathbf{r}_j \rightarrow \mathbf{k}_j$ and $\Phi_{\rm CI} \rightarrow \Phi_{\rm CI}^{\mathcal{M}}$. In addition, Eq. (29) shows that, apart from a phase i^l, the LLL orbitals in momentum space retain the same form as the corresponding ones in configuration space, with the following substitutions: $(r, \theta) \longleftrightarrow (k, \varphi)$ and $\Lambda \longleftrightarrow 1/\Lambda$. Consequently, note the following. (i) All the expressions and final results, including the figure plots, for the first, second, and fourth correlations calculated in real space represent also corresponding results in momentum space, the only change being the units of the axes ($1/\Lambda$ versus Λ). (ii) The TOF measurements in the far field [8,49] act as a microscope that magnifies directly the *in situ* many-body wave function.

In deterministic time-of-flight measurements, the N trapped ultracold atoms expand subsequent to a sudden turnoff of the trapping potential, and a snapshot of the free-space traveling N atomic particles is taken in the far field after a time $t_{\rm TOF}$. This step is repeated several thousand times and the compilation of the ensuing snapshots reproduces the modulus square of the Fourier transform of the *in situ* many-body wave function [18]. $t_{\rm TOF}$ is taken long enough so that the size of the compiled ensemble is much larger than its original (confined) size. The TOF far-field real-space coordinates of the particles at time $t_{\rm TOF}$ are given by $\mathbf{r}_j = \hbar\mathbf{k}_j t_{\rm TOF}/M$, with $j = 1, 2 \ldots, N$, where $\hbar\mathbf{k}_j$ is the single-particle momentum at the source (the confining trap). From the above, we note that during the expansion the interatomic interactions can be neglected, whereas prior to the expansion the interactions play a key role in determining the properties of the trapped correlated LLL state [8,49]. In this way, analyses of TOF measurements allow determination of the properties of the many-body state of the confined system via analyses of the all-order (1 to N) momentum-space correlation functions. These momentum correlation functions are indeed the focus of our study. As aforementioned, for the LLL case investigated here, the single-particle Fourier transform in Eq. (29) retains the same functional form on $\mathbf{k}$ as does $\psi_l(\mathbf{r})$ in Eq. (11) on $\mathbf{r}$. As a result, apart of units, the *in situ* real-space and momentum correlations coincide, and the TOF measurements act as a microscope of the *in situ* many-body wave function.

III. LLL SPECTRA AND MAGIC ANGULAR MOMENTA

A primary tool for the classification and for gaining a deeper understanding of the geometric aspects of the intrinsic correlations in the LLL many-body wave functions is the concept of magic angular momenta, introduced and extensively utilized in the treatments of semiconductor quantum dots [21,29–32,50–54].

It is pertinent to note here analogies between the ultracold-atoms case and that of electrons confined in the above-mentioned semiconductor quantum dots. Indeed, in such parabolically confined (i.e., with a harmonic external potential), finite 2D strongly interacting correlated electron-gas structures, the emergence of intrinsic quantum crystalline-like (or molecularlike) features (so-called Wigner molecules, WMs) is traditionally revealed through analysis of second-order correlations in the CI [21,31,32], or center-of-mass separable [55], many-body wave functions, associated with spontaneous symmetry breaking at the mean-field unrestricted Hartree-Fock level [56–58]. At zero magnetic field, formation of such ordered structures has been shown to be

driven by competition between the electron crystallization that minimizes the long-range repulsive Coulomb interelectron interaction and the opposing effect due to the increase in the zero-point kinetic energy that accompanies crystallization (that is, the reduced electron positional uncertainty that occurs due to the localization of the electron at the induced crystalline site) [31,56]. On the other hand, an applied magnetic field is acting as an independent factor inducing WM formation [6,22,31,32]; see also Sec. VII below. The predicted occurrence of such WM electron structures in 2D electron dots under magnetic-field-free conditions, and in the presence of applied magnetic fields (where, as aforementioned, the magnetic-field-induced rotating molecular structures have been termed as rotating Wigner molecules [6,31,59]), have been confirmed experimentally [60–65]. Here, we establish a broader viewpoint by showing that such RWMs emerge also in the case of ultracold fermionic neutral atoms (e.g., ^{6}Li atoms) interacting via short-range contact interactions and confined in a rotating harmonic trap (that is emulating a magnetic field via implementation of a synthetic gauge).

An early [29,30] recognized signature of magic angular momenta was their forming sets of energetically advantageous states (referred to also as cusp states) in the LLL spectra of a few 2D fully spin-polarized electrons. According to subsequent [21,29–32,50–54] findings from CI calculations in the field of semiconductor quantum dots (a few electrons confined in a harmonic potential), the 2D electrons under a perpendicular high magnetic field localize relative to each other and form ordered ringlike configurations $(n_1, n_2, \ldots, n_r)$ (with $\sum_i^r n_i = N$). Such ordered ring configurations are not visible in the CI single-particle densities, which are azimuthally (rotationally) uniform, but are revealed by using higher-order correlations [31]. Furthermore, the CI total angular momenta must be compatible (i.e., satisfy) the C_n point group, etc., symmetries associated with the ring configurations [21,31,32,50–54]. Similar magic angular momenta appear also in the LLL spectra and CI solutions for ultracold bosonic atoms [11]. This paper demonstrates that magic angular momenta are pertinent as well to ultracold fermions in rapidly rotating harmonic traps.

Going beyond the fully spin-polarized case, previous investigations have found [32,52–54] that the magic angular momenta depend in a nontrivial way on the value S of the total spin. In particular, for the case of $N = 4$ fermions (which is the focus of this paper), the associated ringlike configuration is a square (denoted as (0,4) [66]), and the series of magic angular momenta are as follows [53,54]:

$$\begin{aligned} S = 0 &\rightarrow L = 4n \ \text{ or } \ L = 4n + 2, \\ S = 1 &\rightarrow L = 4n - 1 \ \text{ or } \ L = 4n; \ \text{or } \ 4n + 1, \\ S = 2 &\rightarrow L = 4n + 2, \end{aligned} \tag{30}$$

where $n = 0, 1, 2, 3, \ldots$.

The relative ground states of $H_{\rm LLL}$ in each spin sector [see definition below Eq. (6)] are associated with magic angular momenta. Indeed, the values of $L = 2$, 4, and 8 in Fig. 1, corresponding to the ground states in the spin sector ($S = 0$, $S_z = 0$), belong to the $S = 0$ series listed in Eq. (30); note that not all terms in the series given in Eq. (30) correspond to the sequence of ground states of the total Hamiltonian $H_{\rm MB}$. Furthermore, in the spin sector ($S = 2$, $S_z = 0$), the relative ground state has the magic angular momentum $L = 6$ in agreement with the series in Eq. (30); see Fig. 3.

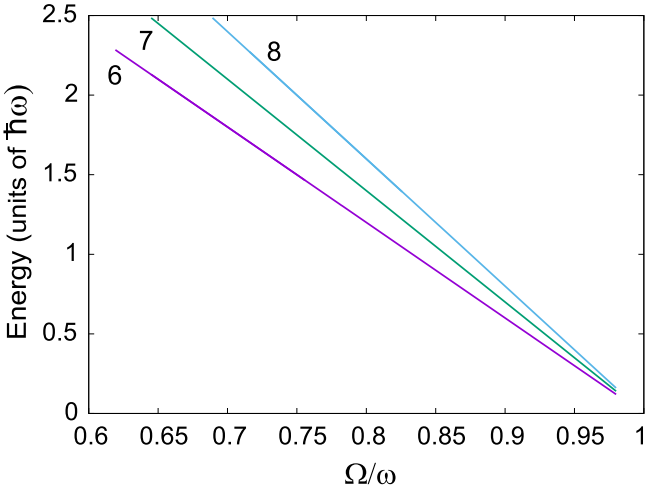

FIG. 3. Spectra of the three lowest-in-energy CI solutions of the many-body Hamiltonian $H_{\rm MB}$ [Eq. (5)] for $N = 4$ fermions as a function of the ratio Ω/ω (the constant energy $N\hbar\omega$ has been subtracted). The spin sector with ($S = 2$, $S_z = 0$) is displayed. The order of the multipole perturbation [see Eq. (6)] $m = 4$ and $R_\delta = 0.4$. Because there are no crossings, only the value $\mathcal{C} = 0.0001$ (weak V_P perturbation) is plotted. The relative ground state has $L = 6$.

To further elaborate on the relation between magic angular momenta and LLL spectra, we display in Fig. 4 the restricted LLL spectra in each spin sector corresponding to the diagonalization of the contact-interaction term only, that is, to the last term in Eq. (2). These spectra are plotted as a function of the total angular momentum L; for each value of L, a tower of excited states is shown (upward standing triangles above the yrast-band line that connects the lowest-energy triangles). These excited LLL states display a highest-energy bound at $2.5R_\delta\hbar\omega$. The number of states in each tower increases with increasing L, and every newly appearing energy at a given L repeats itself at larger L's. In this figure, the lowest energies for each L (forming the so-called yrast band) are highlighted by passing a line through them. For the ($S = 0$, $S_z = 0$) and ($S = 1$, $S_z = 0$) spin sectors, the yrast bands involve successively lower energies and eventually they collapse to a horizontal line at vanishing energy. For the ($S = 2$, $S_z = 0$), only the horizontal segment at zero enery is present. The zero-energy horizontal segment in Fig. 4 is a property connected to the zero range of the contact interaction; it is absent in the case of the long-range Coulomb interaction [21,31,54].

In Fig. 4, the magic angular momenta according to Eq. (30) are marked by an arrow. They are preceded by a sharp drop in energy relative to the previous angular momentum (as long as the previous L is nonmagic or nonvanishing); as a result, the associated LLL states are often referred to as cusp states [31,67].

For a discussion on the group-theoretical relationship between the geometric structure of a Wigner molecule made of spinful fermions, and the corresponding magic angular momenta sequences for different spin states of the WM,

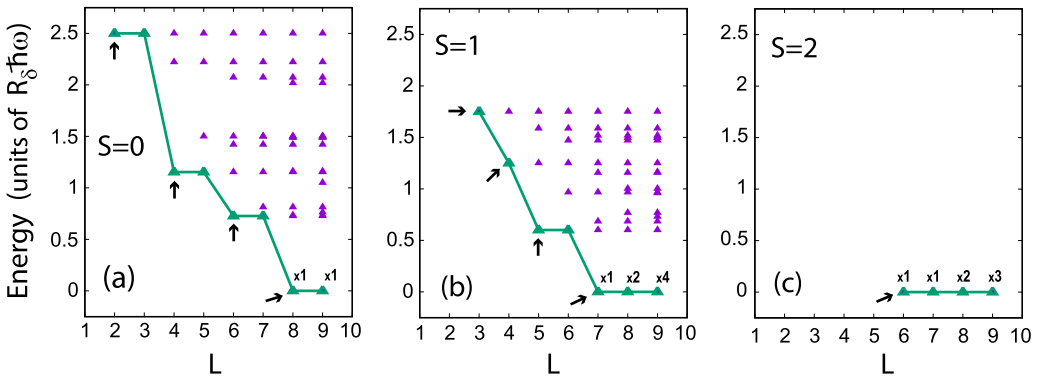

FIG. 4. CI-calculated, partial LLL energy spectra for $N = 4$ fermions deriving from the diagonalization of the contact-interaction term only; see third term of the $H_{\rm LLL}$ Hamiltonian in Eq. (2). (a) The spectrum of the ($S = 0,\ S_z = 0$) sector. (b) The spectrum of the ($S = 1,\ S_z = 0$) sector. (c) The spectrum of the ($S = 2,\ S_z = 0$) sector. The CI spectra were calculated for $S_z = 0$; however, note that these LLL spectra are independent of the precise value of S_z. The arrows indicate magic angular momenta. The symbols $\times n$, with n being an integer, denote the degeneracy of the vanishing-energy states in each spin sector. The horizontal axis represents the total angular momentum L. Energies in units of $R_\delta\hbar\omega$.

we refer the reader to the illustrative example given in Appendix A.

IV. SPIN SECTOR ($S = 0,\ S_z = 0$): TRAVERSING THE AVOIDED CROSSING

In this section, the properties of the relative-ground-state wave functions in the spin sector ($S = 0,\ S_z = 0$) and for $N = 4$ fermions will be investigated in detail along the avoided crossings highlighted in the insets (labeled as A and B) of Fig. 1. The tools used in this analysis are the single-particle densities (first-order correlations) and the N-body correlations (fourth-order for $N = 4$ fermions) defined in Sec. II C.

A. Single-particle densities

In Fig. 5, we plot the CI single-particle density for two different strengths of the pertubation V_P [$\mathcal{C} = 0.004$, top row Figs. 5(a)–5(d) and $\mathcal{C} = 0.0001$, bottom row Figs. 5(e)–5(h)] and for two different values of the rotational frequency across the avoided crossing highlighted in the insets of Fig. 1, i.e., near the midpoint at $\Omega/\omega = 0.8855$ [Figs. 5(a) and 5(b)], or $\Omega/\omega = 0.8847$ [Figs. 5(e) and 5(f)], and after the crossing at $\Omega/\omega = 0.90$ [Figs. 5(c), 5(d), 5(g), and 5(h)]. As was the case in Fig. 1, $R_\delta = 0.4$ and $m = 4$ (hexadecapole multipolarity); for the case of a quadrupolar trap deformation ($m = 2$), see Sec. IV E below. We note again that, in the LLL, the formation of geometric structures of the particles in the trap and their symmetries does not depend on the precise value of R_δ (see also discussion in Sec. VII below).

As seen from Figs. 5(a)–5(d), the value $\mathcal{C} = 0.004$ is rather large and results in a symmetry-broken solution even at the point $\Omega/\omega = 0.90$. Indeed, at this point, the associated expectation value of the total angular momentum $\langle L\rangle = 8.0364$ is still rather different from the integer value of 8. On the contrary, the small value $\mathcal{C} = 0.0001$ yields $\langle L\rangle = 8.00002$ at $\Omega/\omega = 0.90$, and the corresponding many-body wave function preserves the rotational symmetry for all practical purposes; see the single-particle density in Fig. 5(g).

This behavior conforms with the fact that the many-body wave functions $\Phi_{\rm gs}$'s, associated with Figs. 5(a) and 5(b), 5(c) and 5(d), and 5(e) and 5(f) contain significant contributions of basis determinants with total angular momenta other than $L = 8$, i.e., $L = 4$ and 12; see Tables STI– STIV in the Supplemental Material (SM) [68]. In contrast, the many-body wave function $\Phi_{\rm gs}$ associated with Figs. 5(g) and 5(h) consists mainly of basis determinants each with total angular momentum $L = 8$ (with one exception of a basis determinant of $L = 4$ having a very small weight); see Table STIV in the SM [68].

It is remarkable that in all cases of symmetry breaking portrayed by the 3D surfaces in Figs. 5(a), 5(c), and 5(e), the same underlying Wigner-molecule, square-ring configuration emerges. This (0,4) ring configuration is further highlighted by plotting the corresponding cuts through the origin along the diagonals (solid line, violet) and perpendicular to the sides (dashed line, green) of the square configuration in Figs. 5(b), 5(d), 5(f), and 5(h), respectively. In Fig. 5(h), the reestablishment of rotational symmetry is reflected in the fact that both the solid and dashed cuts do overlap. Furthermore, the demonstrated here effect of V_P at the avoided crossing upon the CI single-particle density is so profound and disproportionate to the smallness of the perturbation [compare, e.g., Figs. 5(e) and 5(g)] that it is appropriate to characterize the present results as a numerical example of the "flea on the elephant" concept [69–71], developed in mathematical treatments of the phenomenon of spontaneous symmetry breaking [72].

B. Fourth-order correlations associated with the symmetry-preserving $L = 8$ relative ground state

A deeper understanding of the interplay, portrayed in Fig. 5, between symmetry-broken solutions and those that preserve the 2D rotational symmetry is gained by considering the fourth-order correlations defined in Sec. II C. Figure 6 displays the spin-unresolved fourth-order correlations [see Eq. (26)] associated with Fig. 5(g), i.e., for $\mathcal{C} = 0.0001$ at the point $\Omega/\omega = 0.90$. The most natural way to analyze this quantity, that depends on four variables, is to fix three variables

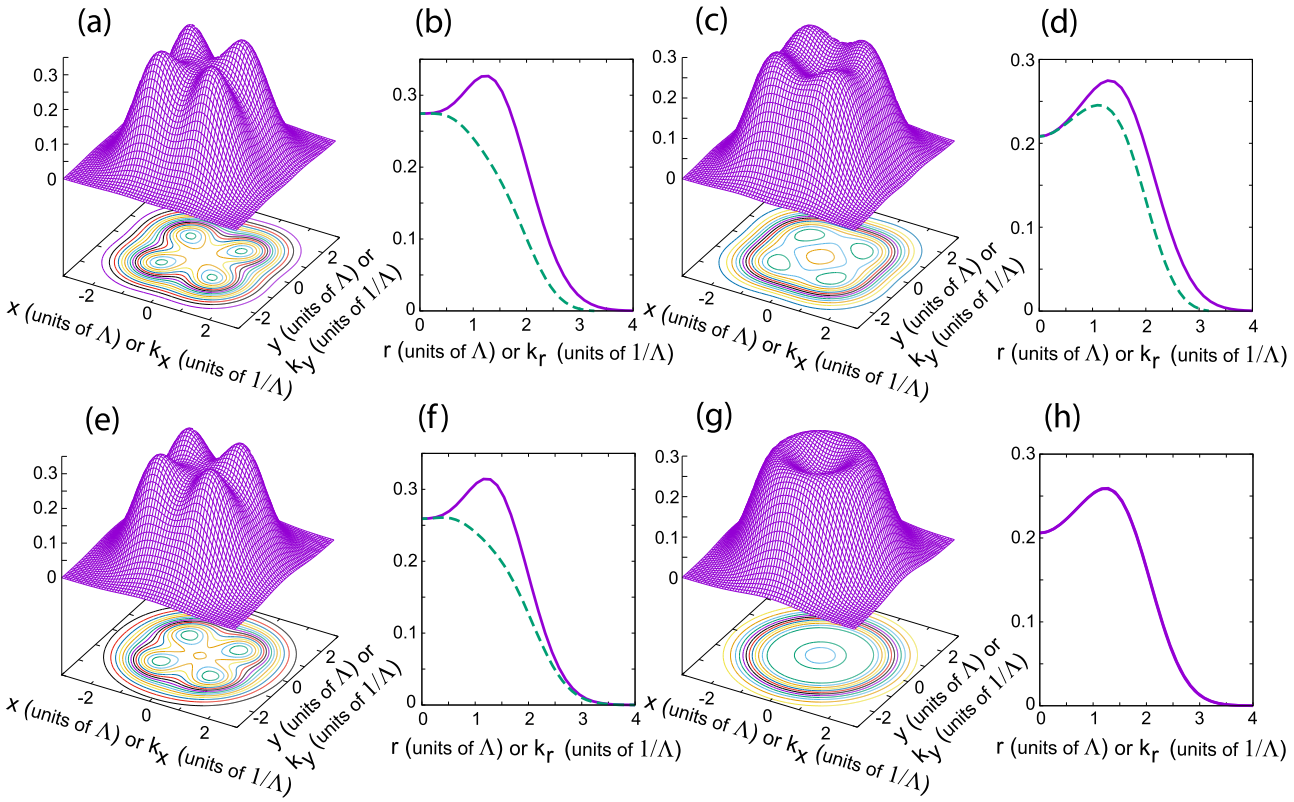

FIG. 5. CI single-particle densities (both in real space and momentum space) of the relative ground state of $N = 4$ fermions in the spin sector with ($S = 0$, $S_z = 0$). 3D surfaces are plotted in (a), (c), (e), and (g). Corresponding cuts through the origin along the diagonals (solid line, violet) and perpendicular to the sides (dashed line, green) of the square configuration are displayed in (b), (d), (f), and (h), respectively. In (h) both curves overlap. (a), (b) Calculation for $\mathcal{C} = 0.004$ (strong perturbation) at the point $\Omega/\omega = 0.8855$. The expectation value of the total angular momentum is $\langle L\rangle = 7.189$, indicating that the plotted case is a state with broken rotational symmetry. (c), (d) Calculation for $\mathcal{C} = 0.004$ (strong perturbation) at the point $\Omega/\omega = 0.90$. The expectation value of the total angular momentum is $\langle L\rangle = 8.0364$, closer to integer 8, but the broken rotational symmetry is still present. (e), (f) Calculation for $\mathcal{C} = 0.0001$ (weak perturbation) at the point $\Omega/\omega = 0.8847$. The expectation value of the total angular momentum is $\langle L\rangle = 7.330$, and the single-particle density exhibits strong breaking of the rotational symmetry. (g), (h) Calculation for $\mathcal{C} = 0.0001$ (weak perturbation) at the point $\Omega/\omega = 0.90$. The expectation value of the total angular momentum is $\langle L\rangle = 8.00002$, very close to integer 8, and the rotational symmetry is practically reestablished. $R_\delta = 0.4$ and the order of the multipole trap deformation $m = 4$. Because of the properties of the Fourier transform of the LLL orbitals [see Eq. (29)], both real-space and momentum densities are given by the same 3D numerical surface. For the spatial densities, the lengths along the x, y, and r axes are given in units of Λ, and the vertical axes are in units of $1/\Lambda^2$. For the momentum densities, the momenta along the k_x, k_y, and k_r axes are given in units of $1/\Lambda$, and the vertical axes are in units of Λ^2.

and plot ${}^4\mathcal{G}_{\rm gs}$ as a function of the fourth variable. Motivated by the molecular ring configuration [usually denoted as (0,4)] of the broken-symmetry single-particle densities, we place the three fixed variables at the points $r_0\exp(j\pi/2+\Theta)$ (with $j = 1, 2, 3$), where $r_0 = 1.22\ \Lambda$ is the radius of the maxima of the four humps in Fig. 5(e), the angle $\pi/2$ reflects the square arrangement of these four humps, and Θ is an arbitrary reference angle. Two values of $\Theta = 0$ [Fig. 6(a)] and $\Theta = \pi/4$ [Fig. 6(b)] were used. In both cases, Fig. 6 shows that the conditional probability of finding the fourth fermion at a given point is localized around the apex point that completes the square of the (0,4) ring configuration.

Naturally, the fact that the intrinsic (0,4) molecular configuration contained in the ${}^4\mathcal{G}_{\rm gs}$ correlation is independent of the reference angle Θ is consistent with the uniform (2D rotationally symmetric) single-particle density in Fig. 5(g); it is also the property that suggests the characterization of the associated many-body state as a "rotating Wigner molecule" [59], in contrast to the term "pinned Wigner molecule" suggested by the broken-symmetry single-particle densities in Figs. 5(a), 5(c), and 5(e).

C. Second-order correlations associated with the symmetry-preserving $L = 8$ relative ground state

As described in Sec. II C, second-order correlations are a complementary tool in obtaining information regarding the intrinsic structure of the many-body wave function in the absence of symmetry breaking. The second-order correlations [see Eqs. (17) and (18)] for the symmetry-preserving relative ground state in the ($S = 0$, $S_z = 0$) spin sector at $\Omega/\omega = 0.90$ with $m = 4$ and $\mathcal{C} = 0.0001$ [corresponding to the single-particle density in Fig. 5(g)] are displayed in Fig. 7. Specifically, taking the fixed point at $\mathbf{r}_0 = (1.22\Lambda, 0)$, Figures 7(a) and 7(b) portray the up-up, ${}^2\mathcal{G}_{\uparrow\uparrow}$, and up-down, ${}^2\mathcal{G}_{\uparrow\downarrow}$, spin-resolved second-order correlations, respectively, whereas

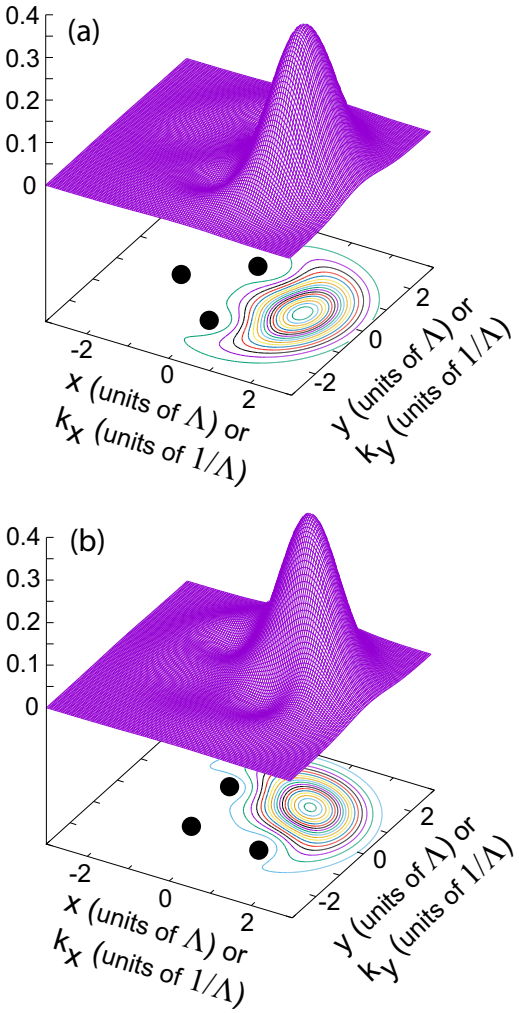

FIG. 6. Unresolved fourth-order correlations (both in real space and momentum space) of the relative CI ground state in spin sector ($S = 0$, $S_z = 0$) for $N = 4$ fermions at the trap angular frequency $\Omega/\omega = 0.90$. The strength of the V_P perturbation is weak with $\mathcal{C} = 0.0001$. $R_\delta = 0.4$, and the order of the multipole trap deformation $m = 4$. These correlations correspond to the 2D rotationally symmetric single-particle density in Fig. 5(g). The three fixed points (denoted by the solid dots) are placed at a radius $r_0 = 1.22\ \Lambda$. The reference angle $\Theta = 0$ in (a) and $\Theta = \pi/4$ in (b). Because of the properties of the Fourier transform of the LLL orbitals [see Eq. (29)], both real-space and momentum fourth-order correlations are given by the same 3D numerical surface. For the spatial correlations, the lengths along the x and y axes are given in units of Λ, and the vertical axes are in units of $1/(\pi^4\Lambda^8)$. For the momentum correlations, the momenta along the k_x and k_y axes are given in units of $1/\Lambda$, and the vertical axes are in units of Λ^8/π^4. In the case of the momentum correlations, r_0 here is replaced by $k_r^0 = 1.22\ 1/\Lambda$. Corresponding mappings between the fixed points of the real-space and momentum-space correlations apply also for Figs. 7, 9(b), 10, and 11 below.

Fig. 7(c) portrays the spin-unresolved one. Figures 7(d) and 7(e) portray the up-up and up-down second-order correlations, respectively, but with the fixed point taken to be at the origin. Lastly, Fig. 7(f) displays the difference between the two spin-resolved correlations ${}^2\mathcal{G}_{\uparrow\downarrow} - {}^2\mathcal{G}_{\uparrow\uparrow}$ when the fixed point is taken at the origin.

In addition to reproducing the relative single-particle localization of the four fermions in a square configuration (discussed in Sec. IV B using fourth-order correlations), the second-order correlations in Figs. 7(a) and 7(b) can assist in the determination of the underlying spin structure of the corresponding many-body wave function. To this end, the six ζ_i's spin primitives [see Eq. (22)], associated with the Wigner-molecule square geometry are depicted graphically in the inset of Fig. 7.

According to Fig. 7(a), when the fixed spin-up fermion is placed at one corner of the square, the most probable locations of the other spin-up fermion are the two adjacent corners of the square, but not the opposite corner along the diagonal. This behavior is consistent with the graphical depictions of ζ_1 and ζ_3 (or ζ_4 and ζ_6). In addition, it is straightforward to see that the $\uparrow\downarrow$ second-order correlation in Fig. 7(b) is consistent with the same graphics for ζ_1 and ζ_3 (or ζ_4 and ζ_6). Indeed, the most probable locations for the down-spin fermions are all three remaining corners, including the one across the diagonal. The higher probability at the corner across the diagonal is accounted for by the fact that this corner appears in both graphics as probable location of the down fermions. Taking into consideration that ${}^2\mathcal{G}_{\downarrow\downarrow} =^2 \mathcal{G}_{\uparrow\uparrow}$ and ${}^2\mathcal{G}_{\downarrow\uparrow} =^2 \mathcal{G}_{\uparrow\downarrow}$, one can conclude that the dominant contributions in the many-body wave function contain the spin configuration

$$\zeta_1 - \zeta_3 - \zeta_4 + \zeta_6, \tag{31}$$

the minus signs resulting from the requirement that the spin function in Eq. (31) must be an eigenstate of the total spin with $S = 0$.

The spin-unresolved ${}^2\mathcal{G}_{\text{unres}}$ in Fig. 7(c) is the sum of all four spin-resolved correlations ${}^2\mathcal{G}_{\uparrow\uparrow}$, ${}^2\mathcal{G}_{\downarrow\downarrow}$, ${}^2\mathcal{G}_{\uparrow\downarrow}$, and ${}^2\mathcal{G}_{\downarrow\uparrow}$, a fact that is reflected in the difference in the scales for the vertical axes going from Fig. 7(a) to Fig. 7(c); note that there are two spin-down, but only one spin-up, other fermions for any given spin-up fermion. Furthermore, although weakened, due to the overlap of the different components that are added up, the (0,4) square ringlike geometry is recognizable in Fig. 7(c), as well.

Comparing the bottom row of panels in Fig. 7 [i.e., panels (d), (e), and (f)] with the top row of panels in the same figure, it is apparent that placing the fixed point $\mathbf{r}_0$ at the origin misses crucial information concerning the many-body wave function, that is, it misses both the presence of the spin function displayed in Eq. (31), as well as the emergence of a square-ring Wigner-molecule configuration.

D. Spin structure of the symmetry-preserving $L = 8$ relative ground state

Motivated by the analysis of the second-order correlations in Sec. IV C, showing that the spin function displayed in Eq. (31) must be an important component of the many-body CI wave function $\Phi_{\text{CI}}^{L=8,S=0,S_z=0}$, it is instructive to interrogate whether the complete spin function of this state can be determined from the miscroscopic CI wave function. To this end, we use the $c(J)$ coefficients (rounded to the fourth decimal point) listed in Table STIV in the SM [68]; naturally, we neglect the two orders-of-magnitude smaller $c(2)$ coefficient. With the above, the CI wave function can be approximated by

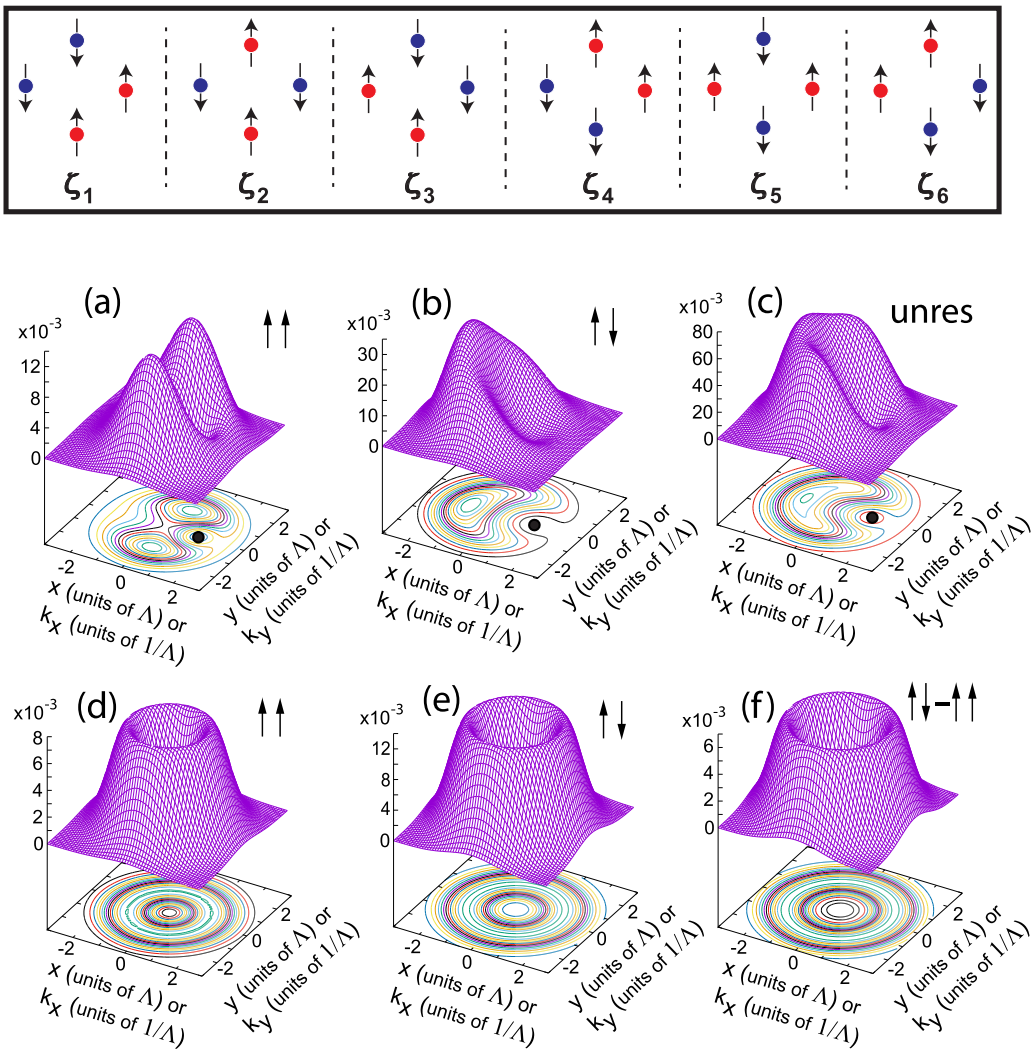

FIG. 7. ↑↑ (a), (d), ↑↓ (b), (e), and spin-unresolved (c) second-order correlations (both in real space and momentum space) of the relative CI ground state in spin sector ($S = 0,\ S_z = 0$) with $L = 8$ for $N = 4$ fermions at the trap angular frequency $\Omega/\omega = 0.90$. The strength of the V_P perturbation is weak, using $\mathcal{C} = 0.0001$ with $m = 4$ and $R_\delta = 0.4$. These correlations correspond to the 2D rotationally symmetric single-particle density in Fig. 5(g). (d) The difference ${}^2\mathcal{G}_{\uparrow\downarrow} - {}^2\mathcal{G}_{\uparrow\uparrow}$. The fixed points (see text) are placed at ($x_0 = 1.22\ \Lambda,\ y_0 = 0$) for the three top panels, and at the origin ($x_0 = 0,\ y_0 = 0$) for the three bottom panels. Because of the properties of the Fourier transform of the LLL orbitals [see Eq. (29)], both real-space and momentum correlations are given by the same 3D numerical surface. For the space correlations, the lengths along the x and y axes are given in units of Λ, and the vertical axes are in units of $1/\Lambda^4$. For the momentum correlations, the momenta along the k_x and k_y axes are given in units of $1/\Lambda$, and the vertical axes are in units of Λ^4. In (a)–(c), the fixed point is denoted by a solid dot. The inset provides a graphical representation of the six ζ_i's spin primitives [see Eq. (22)], when associated with the Wigner-molecule square geometry.

the sum of 15 Slater determinants (specified in Table STIV by the single-particle angular momenta l_i, with $i = 1, \ldots, 4$), whose CI coefficients obey the following relations:

$$\begin{aligned} &c(1) = c(16) = 2c(4) = -2c(6) = -2c(9) = 2c(11) = c_1, \\ &c(3) = c(15) = c_2, \quad 2c(8) = 2c(14) = -c_2, \\ &c(5) = c(13) = c_3, \quad c(7) = c(12) = c_4, \quad c(10) = c_5. \end{aligned} \tag{32}$$

From Table STIV in the SM, one can extract numerical values for the five constants c_i (with $i = 1, \ldots, 5$) in Eq. (32). However, as we will discuss below, the spin structure is independent of specific numerical values. Note that the coefficients grouped together in each line of Eq. (32) are associated with given (nonordered) sets of single-particle angular momenta l_i, i.e., with the six sets (0,1,3,4), (0,2,2,4), (1,2,2,3), (0,3,2,3), (1,2,1,4), and (1,3,1,3), respectively.

Using the relations (32) and the 15 Slater determinants in Table STIV in the SM [68], and employing the MATHEMATICA algebraic language [73] we can write the CI wave function in the form of Eq. (23). The analytic expressions of the space parts $\mathcal{F}_i(z_1, z_2, z_3, z_4)$ (with $i = 1, \ldots, 6$ and $z = x + iy = re^{i\theta}$) are lengthy to be explicitly written in the text. However, the interested reader will find them as MATHEMATICA scripts in the Supplemental Material [68].

Before proceeding with the analysis, we recall here the form of the six spin eigenfunctions $\widetilde{\zeta}_i$ (with $i = 1, \ldots, 6$)

having both good total spin S and a good spin projection S_z. These spin eigenfunctions can be obtained by solving a four-site Heisenberg Hamiltonian with the four spins arranged in a closed rectangular configuration, as was done in Appendix B of Ref. [74]. Taking all four Heisenberg exchange constants to be equal, the spin eigenfunctions (B13)–(B18) in Ref. [74] simplify to the following (relevant to this paper) expressions:

$$\widetilde{\zeta}_1 = \frac{1}{\sqrt{12}}(\zeta_1 + \zeta_3 + \zeta_4 + \zeta_6 - 2\zeta_2 - 2\zeta_5), \quad S = 0, \tag{33}$$

$$\widetilde{\zeta}_2 = \frac{1}{2}(\zeta_1 - \zeta_3 - \zeta_4 + \zeta_6), \quad S = 0, \tag{34}$$

$$\widetilde{\zeta}_3 = \frac{1}{\sqrt{2}}(\zeta_6 - \zeta_1), \quad S = 1, \tag{35}$$

$$\widetilde{\zeta}_4 = \frac{1}{\sqrt{2}}(\zeta_5 - \zeta_2), \quad S = 1, \tag{36}$$

$$\widetilde{\zeta}_5 = \frac{1}{\sqrt{2}}(\zeta_4 - \zeta_3), \quad S = 1, \tag{37}$$

$$\widetilde{\zeta}_6 = \frac{1}{\sqrt{6}}(\zeta_1 + \zeta_2 + \zeta_3 + \zeta_4 + \zeta_5 + \zeta_6), \quad S = 2, \tag{38}$$

where the ζ_i's (with $i = 1, \ldots, 6$) were defined in Eq. (22).

Solving the system of Eqs. (33)–(38) to obtain the spin primitives ζ_i (with $i = 1, \ldots, 6$), as a function of the spin eigenfunctions $\widetilde{\zeta}_j$ (with $j = 1, \ldots, 6$), one can rearrange Eq. (23) for the many-body wave function as follows:

$$\Phi_{\rm CI} = \sum_{i=1}^{6} \mathcal{F}_i \zeta_i = \sum_{i=1}^{6} \widetilde{\mathcal{F}}_i \widetilde{\zeta}_i, \tag{39}$$

where

$$\widetilde{\mathcal{F}}_1 = \frac{1}{\sqrt{12}}(\mathcal{F}_1 + \mathcal{F}_3 + \mathcal{F}_4 + \mathcal{F}_6 - 2\mathcal{F}_2 - 2\mathcal{F}_5), \quad S = 0, \tag{40}$$

$$\widetilde{\mathcal{F}}_2 = \frac{1}{2}(\mathcal{F}_1 - \mathcal{F}_3 - \mathcal{F}_4 + \mathcal{F}_6), \quad S = 0, \tag{41}$$

$$\widetilde{\mathcal{F}}_3 = \frac{1}{\sqrt{2}}(\mathcal{F}_6 - \mathcal{F}_1), \quad S = 1, \tag{42}$$

$$\widetilde{\mathcal{F}}_4 = \frac{1}{\sqrt{2}}(\mathcal{F}_5 - \mathcal{F}_2), \quad S = 1, \tag{43}$$

$$\widetilde{\mathcal{F}}_5 = \frac{1}{\sqrt{2}}(\mathcal{F}_4 - \mathcal{F}_3), \quad S = 1, \tag{44}$$

$$\widetilde{\mathcal{F}}_6 = \frac{1}{\sqrt{6}}(\mathcal{F}_1 + \mathcal{F}_2 + \mathcal{F}_3 + \mathcal{F}_4 + \mathcal{F}_5 + \mathcal{F}_6), \quad S = 2. \tag{45}$$

We note that the arrangement of the $\widetilde{\mathcal{F}}_i$'s in Eqs. (40)–(45) coincide with that of the ζ_i's in Eqs. (33)–(38).

Using the analytic expressions [68] for the $\mathcal{F}$'s, one can verify that $\widetilde{\mathcal{F}}_3 = \widetilde{\mathcal{F}}_4 = \widetilde{\mathcal{F}}_5 = \widetilde{\mathcal{F}}_6 = 0$, which is a confirmation of the fact that the CI wave function under consideration has total spin $S = 0$. Consequently, one obtains the following general form for the $L = 8$ ground state in the spin sector ($S = 0,\ S_z = 0$):

$$\Phi_{\rm CI}^{L=8,S=0,S_z=0} = \widetilde{\mathcal{F}}_1 \widetilde{\zeta}_1 + \widetilde{\mathcal{F}}_2 \widetilde{\zeta}_2. \tag{46}$$

From the analysis of second-order correlations in Sec. IV C, it follows that the contribution of the first term in Eq. (46) must be less important than that of the second term. Indeed, this can further be confirmed by choosing the four spatial coordinates to adhere to a square arrangement, i.e., by taking $z_1 = z_0$, $z_2 = z_0 e^{i\pi/2}$, $z_2 = z_0 e^{i\pi}$, and $z_2 = z_0 e^{i3\pi/2}$, with the point z_0 being arbitrary. In this case, the spin structure of $\Phi_{\rm CI}^{L=8,S=0,S_z=0}$ agrees with Eq. (31), i.e., one finds

$$\widetilde{\mathcal{F}}_1 = 0,$$

$$\widetilde{\mathcal{F}}_2 = \frac{3c_1 - 3\sqrt{6}c_2 + 2\sqrt{2}c_3 + 2\sqrt{3}c_4 - 4c_5}{3\pi^2\sqrt{4!}} z_0^L e^{-2z_0^* z_0}, \tag{47}$$

where of course $L = 8$ here.

We further note that both $\widetilde{\mathcal{F}}_1$ and $\widetilde{\mathcal{F}}_2$ may contain the associated Vandermonde determinant as a factor, like an assumption [75] used earlier in the description of quantal versions of skyrmions. Naturally, the Fock antisymmetrization here is guaranteed by the fact that $\Phi_{\rm CI}^{L=8,S=0,S_z=0}$ is the sum of Slater determinants.

E. Pinning the Wigner molecule with a quadrupolar perturbation ($m = 2$)

The "flea on the elephant" behavior [69–71] played by the small perturbation in the emergence of the pinned and symmetry-broken WM was described in Sec. IV A. This behavior can be further illustrated by considering a V_P with a multipolarity incommensurate to the intrinsic hexadecapole ($m = 4$) multipolarity of the square Wigner molecule, associated with $N = 4$ fermions. To this effect, a quadrupolar multipolarity (i.e., $m = 2$) is most relevant because it may facilitate experimental endeavors.

In this context, Fig. 8 displays the CI single-particle densities for $N = 4$ LLL fermions at rotational frequencies located inside the region of the avoided crossing from angular momentum $L = 4$ to 8, but with the exact diagonalization of the many-body Hamiltonian (including V_P) performed with $m = 2$ in Eq. (6). It is seen that for a weak perturbation ($\mathcal{C} = 0.0002$) the configuration of the Wigner molecule remains unaltered, exhibiting its intrinsic square geometry; see Fig. 8(a). For stronger perturbations (e.g., $\mathcal{C} = 0.004$), the Wigner molecule starts feeling the details of the external perturbation and, naturally, it exhibits a slight rectangular deformation from the perfect square configuration; see Fig. 8(b).

V. SPIN SECTOR ($S = 2,\ S_z = 0$): AN ANALOG OF THE (1,1,1) HALPERIN STATE

Focusing now on the spin sector ($S = 2,\ S_z = 0$), we note that all the eigenvalues $E_{\rm int}$ associated with the contact-interaction term of the $H_{\rm LLL}$ Hamiltonian [third term in Eq. (2)] are vanishing [see Fig. 4(c)], so that the curves in Fig. 3 are nonintersecting straight lines, converging to zero for $\Omega/\omega = 1$. The relative ground state has a total angular momentum $L = 6$, which is of interest because it coincides with the angular momentum of the trial wave function [denoted as (1,1,1)] proposed by Halperin [4] for spinful fermions as a generalization of the celebrated Laughlin wave function [3] (applicable only for the case of fully spin-polarized fermions). Indeed, the general (p, p, q) Halperin wave function, where p

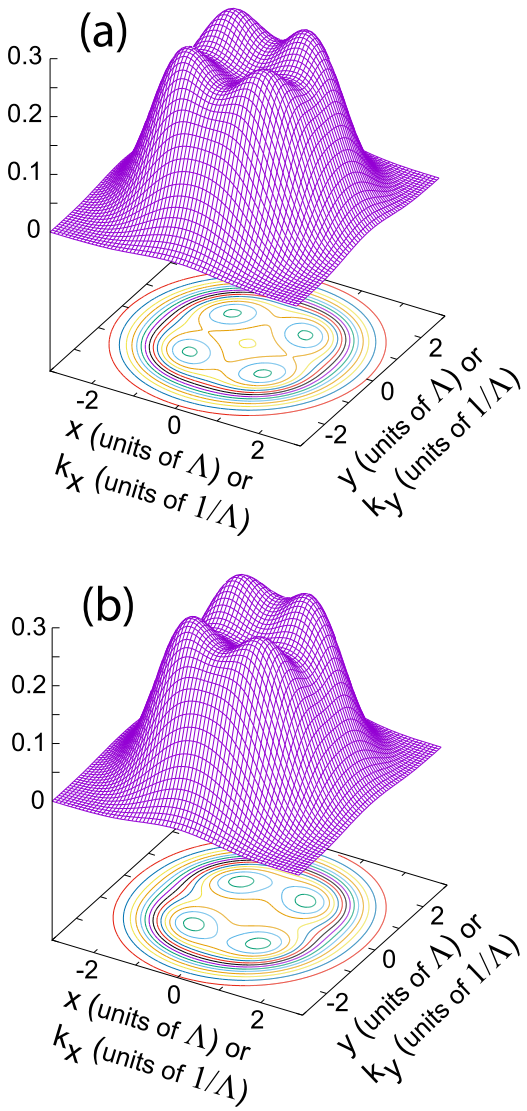

FIG. 8. CI single-particle densities (both in real space and momentum space) of the relative ground state of $N = 4$ fermions in the spin sector with ($S = 0$, $S_z = 0$), but considering a quadrupolar perturbation ($m = 2$), in contrast to the hexadecapole perturbation in Fig. 5. $R_\delta = 0.40$. 3D surfaces are plotted. (a) Calculation for $\mathcal{C} = 0.0002$ (weak perturbation) at the point $\Omega/\omega = 0.884\,651$. The expectation value of the total angular momentum is $\langle L\rangle = 7.8501$, indicating that the plotted case is a state with broken rotational symmetry. (b) Calculation for $\mathcal{C} = 0.004$ (strong perturbation) at the point $\Omega/\omega = 0.885$. The expectation value of the total angular momentum is $\langle L\rangle = 7.8252$. For the spatial densities, the vertical axes are in units of $1/\Lambda^2$. For the momentum densities, the vertical axes are in units of Λ^2.

and q are positive integers, is given by [4,76,77]

$$\Upsilon_{(p,p,q)}(z,w) = \prod_{i<j}^{N_\uparrow}(z_i - z_j)^p \prod_{k<l}^{N_\downarrow}(w_k - w_l)^p \prod_{i,k}^{N_\uparrow,N_\downarrow}(z_i - w_k)^q. \quad (48)$$

In Eq. (48), $z_i = r_i e^{i\theta_i}$ and $w_k = r_k e^{i\theta_k}$ are the space coordinates (here in units of Λ) in the complex plane for the spin-up and -down fermions, respectively. Note further that the trivial Gaussian factors $\exp[-\sum_{i=1}^{N_\uparrow} z_i^* z_i/2]\exp[-\sum_{k=1}^{N_\downarrow} w_k^* w_k/2]$ have been omitted in Eq. (48). The total angular momentum associated with the wave function $\Upsilon_{(p,p,q)}(z,w)$ is [78]

$$L_{(p,p,q)} = p\frac{N_\uparrow(N_\uparrow-1)}{2} + p\frac{N_\downarrow(N_\downarrow-1)}{2} + qN_\uparrow N_\downarrow, \quad (49)$$

which indeed for $N_\uparrow = N_\downarrow = 2$ and $p = q = 1$ gives $L_{(1,1,1)} = 6$.

Of significance is the fact that the original proposal for the $\Upsilon(z,w)$ wave functions did not include the spin variables. Below, we will investigate the connection of the (1,1,1) Halperin wave function to the CI many-body wave function which is the relative ground state in the ($S = 2$, $S_z = 0$) spin sector [79]; recall that the relative ground state is the lowest-in-energy state within each spin sector. Furthermore, using this connection we will demonstrate a two-dimensional case of *mapping* from spinful to spinless fermions that is analogous to the fermionization mapping in one dimension [34].

A. Fourth-order correlation and the molecular configuration

First in Fig. 9 we display the single-particle density [Fig. 9(a)] and the corresponding spin-unresolved fourth-order correlation [Fig. 9(b)] for the CI state with $S = 2$, $S_z = 0$ and $L = 6$. It is seen that the single-particle density is rotationally symmetric, but an intrinsic square geometrical configuration appears in the unresolved fourth-order correlation. This is similar to the behavior found for the CI relative ground state in the spin sector ($S = 0$, $S_z = 0$) at the point $\Omega/\omega = 0.90$. Common to these two states is the fact that the corresponding angular momenta, i.e., $L = 6$ and 8, respectively, are magic ones compatible with the C_4 point-group symmetry; see Eq. (30).

B. Comparison between CI state and trial (1,1,1) Halperin wave function

Furthermore, in Table I, we list the dominant CI coefficients $c(I)$ and the spin orbitals $(l_1\uparrow, l_2\uparrow, l_3\downarrow, l_4\downarrow)$, entering into the associated basis of Slater determinants (see Sec. II B). The criterion used for selection of the most dominant determinants in the CI solution was $|c(I)| > 10^{-3}$. The CI calculation used 1296 basis determinants with all possible total angular momenta from 2 to 30. From Table I, it is apparent that only six determinants with $L = 6$ and equal weighting coefficients $|c(J)|$ contribute to the CI LLL state with $S = 2$, $S_z = 0$; indeed, $\sum_{i=1}^{6}|c(J)|^2 = 0.999\,994\,75$, i.e., the corresponding normalization constant differs from unity only in the sixth decimal point.

Taking into consideration that the numerical value of the $|c(J)|$'s in Table I equals $1/\sqrt{6}$, up to the sixth decimal point, and that the LLL single-particle orbitals [with lengths in units of Λ, the harmonic confinement oscillator length, see text below Eq. (11)] are written as $z^l \exp[-z^*z/2]/\sqrt{\pi l!}$, one can verify the following algebraic identity:

$$\begin{aligned}\Phi_{\rm CI}^{S=2,\,S_z=0} &= \sum_{J=1}^{6}\frac{\mathrm{sgn}(J)}{\sqrt{4!}\sqrt{6}\sqrt{2!3!}\pi^2} \times \mathrm{Det}\left[z_1^{l_1(J)}\alpha(1), z_2^{l_2(J)}\alpha(2), z_3^{l_3(J)}\beta(3), z_4^{l_4(J)}\beta(4)\right] \\ &= -\frac{1}{2\sqrt{3\times 4!}\pi^2}\left(\prod_{i<j}^{4}(z_i - z_j)\right)\frac{\sum_{J=1}^{6}\zeta_J}{\sqrt{6}}, \end{aligned} \quad (50)$$

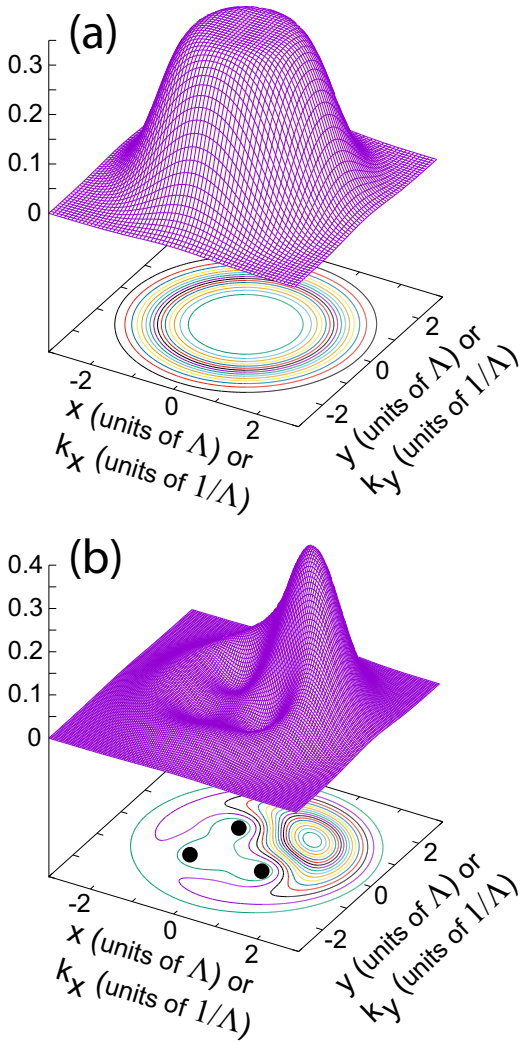

FIG. 9. Structure of the relative CI ground state (in both real space and momentum space) in the spin sector ($S = 2,\ S_z = 0$) for $N = 4$ fermions at the trap angular frequency $\Omega/\omega = 0.90$. (a) Single-particle density. (b) Spin-unresolved fourth-order correlation. The strength of the V_P perturbation is weak with $\mathcal{C} = 0.0001$. $R_\delta = 0.4$, and the order of the multipole trap deformation $m = 4$. Because of the properties of the Fourier transform of the LLL orbitals [see Eq. (29)], both real-space and momentum densities and correlations are given by the same 3D numerical surface. For the spatial quantities, the lengths along the x and y axes are given in units of Λ, and the vertical axes are in units of $1/\Lambda^2$ for the density and $1/(\pi^4\Lambda^8)$ for the fourth-order correlation. For the momentum quantities, the momenta along the k_x and k_y axes are given in units of $1/\Lambda$, and the vertical axes are in units of Λ^2 for the density and Λ^8/π^4 for the the fourth-order correlation. The 2D single-particle density in (a) is rotationally symmetric. In (b), the three fixed points (denoted by solid dots) are placed at a radius $r_0 = 0.90\ \Lambda$, whereas the azimuthal angle between them is $\pi/2$, and the reference angle $\Theta = \pi/4$.

where sgn(J) is the $+$ or $-$ sign of the $c(J)$ coefficients according to Table I. The $\zeta_J,\ J = 1, 2, \ldots, 6$, are defined in Eq. (22), and we omitted the trivial Gaussian factors.

Renaming the spatial coordinates of the spin-up fermions as $z_3 \to w_1$ and $z_4 \to w_2$, one sees immediately that the space part of the $\Phi_{\rm CI}^{S=2,\ S_z=0}$ wave function [see Eq. (50)] coincides with the (1,1,1) Halperin function, i.e., with the expression for $\Upsilon(z, w)$ in Eq. (48) when $p = q = 1$. We recall here the possibility that in certain instances the LLL CI wave function may be expressed exactly in analytical form, as it has been noted in earlier publications [80–82] for the case of LLL ground states of a few spinless bosons in the range $0 \leqslant L \leqslant N$. As a notable counterexample, we mention here the disagreement between the Moore-Read trial wave function [83], which consists mainly of a (0,5) ring configuration, and the CI wave function, which contains mainly a (1,4) ring configuration, in the case of the LLL ground state for $N = 5$ spinless bosons and $L = 8$ [84].

TABLE I. Dominant coefficients $c(I)$ in the CI expansion of the relative LLL ground state (with $L = 6$) in the ($S = 2,\ S_z = 0$) spin sector. The CI expansion ($I = 1, 2, \ldots, I_{\rm total}$) consists of $I_{\rm total} = 1296$ basis determinants. The index J is introduced to relabel the dominant coefficients. The dominance criterion was $|c(I)| > 10^{-3}$.

I	J	$c(J)$	$(l_1\uparrow, l_2\uparrow, l_3\downarrow, l_4\downarrow)$	$\sum_{i=1}^{4} l_i$
16	1	−0.4082472	(0,1,2,3)	6
46	2	0.4082472	(0,2,1,3)	6
81	3	−0.4082472	(0,3,1,2)	6
291	4	−0.4082472	(1,2,0,3)	6
326	5	0.4082472	(1,3,0,2)	6
541	6	−0.4082472	(2,3,0,1)	6

C. What about the second-order correlations?

Unlike the approach in this paper, and a handful of earlier publications [11,82], the second-order correlations have been traditionally considered sufficient (see, e.g., Refs. [3,9,10,20,32,54]) for analyzing the intrinsic structure of the highly correlated LLL states. The case of the ($S = 2,\ S_z = 0$) CI LLL state for $N = 4$ fermions and $L = 6$ shows that the above supposition does not hold in general. Indeed, in Fig. 10, we display the up-up ($\uparrow\uparrow$) and up-down ($\uparrow\downarrow$) spin-resolved second-order correlations for this CI state [which corresponds to the (1,1,1) Halperin wave function]. Note that there is a 1-to-2 ratio between the $\uparrow\uparrow$ and the ($\uparrow\downarrow$) second-order correlations because, for each spin-up fermion, there are one spin-up and two spin-down additional fermions.

As seen from Fig. 10, only the existence of the zero probability for finding two fermions at the same position is visible. Any signature of the square-ring intrinsic molecular structure has been washed away in Fig. 10 due to the averaging performed through the double integrations over the coordinates of the third and fourth particles; see the definition of the second-order correlations in Eq. (18). Revealing the intrinsic Wigner-molecule structure using second-order correlations requires higher total angular momenta, as shown in Ref. [11] for the analogous cases of LLL bosons. However, it appears that the experimental window [20] for a few rapidly rotating ultracold fermions is restricted to the range of small L's, up to values in the neighborhood of $L_{(1,1,1)}$, corresponding to the (1,1,1) Halperin states. Consequently, we conclude that consideration of the N-body correlations offers, as shown in

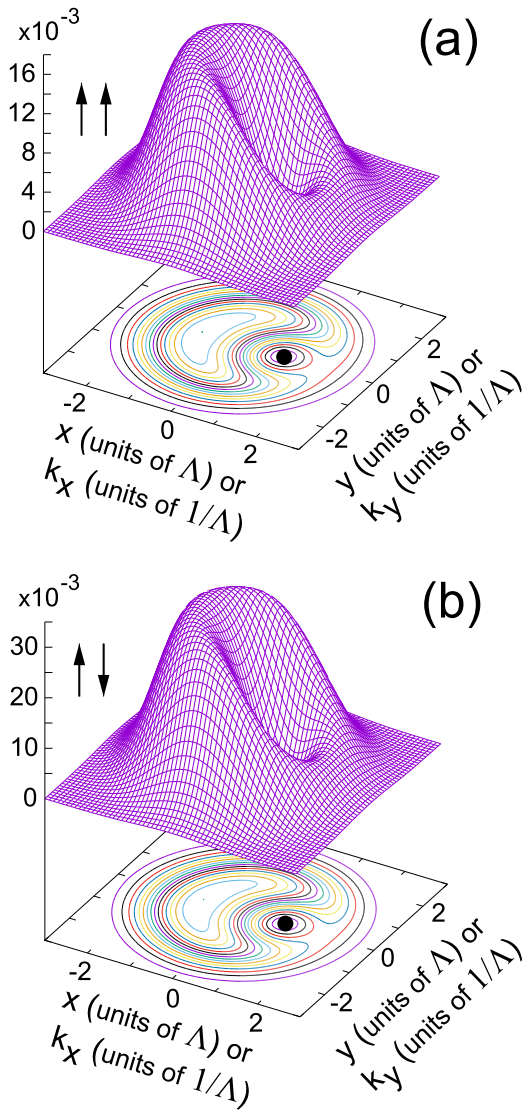

FIG. 10. CI spin-resolved second-order correlations of the relative ground state in the spin sector ($S = 2,\ S_z = 0$) for $N = 4$ fermions at the trap angular frequency $\Omega/\omega = 0.90$. (a) $\uparrow\uparrow$ correlation. (b) $\uparrow\downarrow$ correlation. The strength of the V_P perturbation is weak with $\mathcal{C} = 0.0001$. $R_\delta = 0.4$, and the order of the multipole trap deformation $m = 4$. The fixed point (denoted by a solid dot) was placed at a radius $r_0 = 0.90\ \Lambda$. Because of the properties of the Fourier transform of the LLL orbitals [see Eq. (29)], both real-space and momentum correlations are given by the same 3D numerical surface. For the spatial correlations, the lengths along the x and y axes are given in units of Λ, and the vertical axes are in units of $1/\Lambda^4$. For the momentum correlations, the momenta along the k_x and k_y axes are given in units of $1/\Lambda$, and the vertical axes are in units of Λ^4. Note the different scales between (a) and (b).

this paper, essential additional information regarding the CI wave functions.

VI. A FERMIONIZATION ANALOG IN TWO DIMENSIONS

A. The $L = 6$ state for $N = 4$ fermions

The derivation of the exact CI analytic expression in Eq. (50) enabled us to make another important comparison. It is well known that the fully spin-polarized fermionic LLL CI state with $L = N(N-1)/2 = L_{(1,1,1)}^{N_\uparrow = N_\downarrow}$ consists of only one Slater determinant constructed with the single-particle orbitals $z^0\alpha,\ z^1\alpha,\ldots,z^{N-1}\alpha$ (again the Gaussian factors are omitted). For the case of $N = 4$ fermions, this state is written as (considering that the space part is a Vandermonde determinant)

$$\Phi_{\rm CI}^{S=2,\ S_z=2} = \frac{1}{\sqrt{4!}\sqrt{2!3!}\pi^2}\mathrm{Det}\big[\alpha(1),\ z_2\alpha(2),\ z_3^2\alpha(3),\ z_4^3\alpha(4)\big] = \frac{1}{2\sqrt{3\times 4!}\pi^2}\left(\prod_{i<j}^{4}(z_i - z_j)\right)\alpha(1)\alpha(2)\alpha(3)\alpha(4). \quad (51)$$

One sees that, apart from a sign, the space parts of the spinful $\Phi_{\rm CI}^{S=2,\ S_z=0}$ and the fully spin-polarized $\Phi_{\rm CI}^{S=2,\ S_z=2}$ wave functions are the same. This mapping between a nonpolarized many-body wave function representing *repulsively interacting* fermions and that of fully spin-polarized (equivalent to spinless) *noninteracting* fermions is reminiscent of the well-known mapping [34] in one dimension between the wave function of N hard bosons, i.e., bosons with strong interparticle contact interaction, and that of N noninteracting and spinless fermions; it can be viewed as a generalization of the "fermionization" concept [34] to two dimensions (indeed fermions with different spin projection can coexist in the same position like two bosons).

We note that, because of the exchange hole, the contact interaction becomes inoperative in the case of fully polarized (or spinless) fermions, and as a result this fermionization mapping demonstrates that the intrinsic crystalline correlations portrayed in Fig. 9(b) can be generated, as a limiting case to the quantum Wigner molecule, by the Pauli exclusion principle alone [85].

B. The $L = 15$ state for $N = 6$ fermions

The fermionization analog discussed in Sec. VI A, i.e., the precise mapping between the space parts of the nonpolarized ($S = N/2,\ S_z = 0$) state with $L = N(N-1)/2$ and the corresponding fully polarized ($S = N/2,\ S_z = N/2$) one, is not limited to the $N = 4$ case. Here, we elaborate on another example concerning the more complex LLL state of $N = 6$ fermions with an angular momentum $L = 15$.

As a first step, we establish that the space part of the CI relative ground state for $N = 6$ fermions with $L = 15$ and ($S = 3,\ S_z = 3$) is very well approximated by the Halperin (1,1,1) trial function. To this end, in Table II we list the 20 dominant Slater determinants, out of a total of 7056 ones with various total L's that comprise the basis employed in the actual CI calculation; indeed, $\sum_{i=1}^{20}|c(J)|^2 = 0.999\,982\,0$, i.e., the corresponding normalization constant differs from unity only in the fifth decimal point.

From Table II, two observations are crucial: (1) The coefficients $c(J)$ of these 20 Slater determinants are all equal and their absolute value approximates $1/\sqrt{20} = 0.223\,606\,80$ to the fifth decimal point. (2) Only the six single-particle angular momenta 0, 1, 2, 3, 4, and 5 appear in these dominant Slater determinants, resulting for all of them in a total angular momentum $L = 15$.

TABLE II. The 20 dominant coefficients $c(I)$ in the CI expansion of the relative LLL ground state for $N = 6$ and $L = 15$ in the ($S = 3,\ S_z = 0$) spin sector. The CI expansion ($I = 1, 2, \ldots, I_{\text{total}}$) consists of $I_{\text{total}} = 7056$ basis determinants. The index J is introduced to relabel the dominant coefficients. The dominance criterion was $|c(I)| > 10^{-3}$.

I	J	$c(J)$	$(l_1\uparrow, l_2\uparrow, l_3\uparrow, l_4\downarrow, l_5\downarrow, l_6\downarrow)$	$\sum_{i=1}^{6} l_i$
65	1	−0.22360479	(0,1,2,3,4,5)	15
139	2	0.22360479	(0,1,3,2,4,5)	15
219	3	−0.22360479	(0,1,4,2,3,5)	15
302	4	0.22360479	(0,1,5,2.3.4)	15
628	5	−0.22360479	(0,2,3,1,4,5)	15
708	6	0.22360479	(0,2,4,1,3,5)	15
791	7	−0.22360479	(0,2,5,1,3,4)	15
1123	8	−0.22360479	(0,3,4,1,2,5)	15
1206	9	0.22360479	(0,3,5,1,2,4)	15
1541	10	−0.22360479	(0,4,5,1,2,3)	15
2371	11	0.22360479	(1,2,3,0,4,5)	15
2451	12	−0.22360479	(1,2,4,0,3,5)	15
2534	13	0.22360479	(1,2,5,0,3,4)	15
2866	14	0.22360479	(1,3,4,0,2,5)	15
2949	15	−0.22360479	(1,3,5,0,2,4)	15
3284	16	0.22360479	(1,4,5,0,2,3)	15
4120	17	−0.22360479	(2,3,4,0,1,5)	15
4203	18	0.22360479	(2,3,5,0,1,4)	15
4538	19	−0.22360479	(2,4,5,0,1,3)	15
5377	20	0.22360479	(3,4,5,0,1,2)	15

Taking into consideration that the numerical value of the $|c(J)|$'s in Table II equals $1/\sqrt{20}$, up to the fifth decimal point, and that the LLL single-particle orbitals [with lengths in units of Λ, the harmonic confinement oscillator length, see text below Eq. (11)] are written as $z^l \exp[-z^* z/2]/\sqrt{\pi l!}$, one can verify the following algebraic identity (using the MATHEMATICA scripts given in the Supplemental Material [68]):

$$\Phi^{S=3,\ S_z=0}_{N=6,\ \text{CI}} = \sum_{J=1}^{20} \frac{\text{sgn}(J)}{\sqrt{6!}\sqrt{20}} \text{Det}\big[z_1^{l_1(J)}\alpha(1), z_2^{l_2(J)}\alpha(2), z_3^{l_3(J)}\alpha(3), z_4^{l_4(J)}\beta(4), z_5^{l_5(J)}\beta(5), z_6^{l_6(J)}\beta(6)\big]$$
$$= -\frac{1}{\sqrt{2!3!4!5!}\sqrt{6!}\pi^3}\left(\prod_{i<j}^{6}(z_i - z_j)\right)\frac{\sum_{J=1}^{20} Z_J}{\sqrt{20}}, \tag{52}$$

where we omitted the trivial Gaussian factors. sgn(J) is the + or − sign of the $c(J)$ coefficients according to Table II. The Z_J's, $J = 1, 2, \ldots, 20$, are the spin primitives associated with six spins having an $S_z = 0$ total spin projection. They are defined explicitly in Appendix B.

The $L = 15$ state corresponding to $N = 6$ fully polarized and noninteracting fermions is written as (considering that the space part is a Vandermonde determinant)

$$\sqrt{2!3!4!5!}\sqrt{6!}\pi^3 \Phi^{S=3,\ S_z=3}_{N=6,\ \text{CI}}$$
$$= \text{Det}[\alpha(1), z_2\alpha(2), z_3^2\alpha(3), z_4^3\alpha(4), z_5^4\alpha(5), z_6^5\alpha(6)]$$
$$= \left(\prod_{i<j}^{6}(z_i - z_j)\right)\alpha(1)\alpha(2)\alpha(3)\alpha(4)\alpha(5)\alpha(6). \tag{53}$$

As was the case for $N = 4$ LLL fermions, one sees from Eqs. (52) and (53) that, apart from a sign, the space parts of the spinful $\Phi^{S=3,\ S_z=0}_{N=6,\ \text{CI}}$ and of the fully spin-polarized $\Phi^{S=3,\ S_z=3}_{N=6,\ \text{CI}}$ wave functions are the same, offering another example of the concept of "fermionization" in two dimensions discussed in Sec. VI A.

To complete the inquiry concerning the $L = 15$ relative ground state for $N = 6$ LLL fermions in the spin sector $S = 3$ (with $S_z = 0$ or 3), we investigate its intrinsic symmetries. To this end, we display in Fig. 11 the associated spin-unresolved sixth-order correlation function. Instead of using the numerical result of the CI calculation, we can take advantage of the identity in Eq. (52) and plot the algebraic expression

$$^6\mathcal{G}\big(z, z_2^0, z_3^0, z_4^0, z_5^0, z_6^0\big)$$
$$\propto \big(z - z_2^0\big)\big(z - z_3^0\big)\big(z - z_4^0\big)\big(z - z_5^0\big)\big(z - z_6^0\big)$$
$$\times\big(z^* - z_2^{0*}\big)\big(z^* - z_3^{0*}\big)\big(z^* - z_4^{0*}\big)\big(z^* - z_5^{0^*}\big)\big(z^* - z_6^{0^*}\big). \tag{54}$$

The superscript 0 indicates a fixed point. Two cases are plotted in Fig. 11: in Fig. 11(a) the five fixed points are located on a circle of radius $r_0 = 1.6\ \Lambda$ and form a regular pentagon,

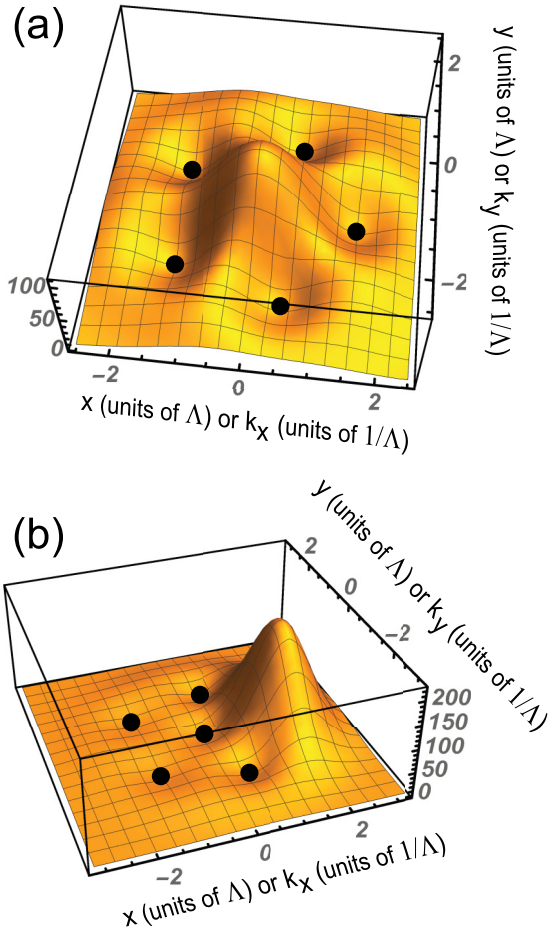

FIG. 11. The ${}^6\mathcal{G}(x, y)$ (with $x + iy = z$) sixth-order spin-unresolved correlation [see Eq. (54)] of $N = 6$ LLL fermions for the relative ground state with $L = 15$ in the spin sector $S = 3$ (with $S_z = 0$ or 3). It exhibits a (1,5) intrinsic geometrical configuration. (a) The fixed points (highlighted by solid dots) are placed at $z_2^0 = r_0$, $z_3^0 = r_0 e^{2\pi i/5}$, $z_4^0 = r_0 e^{4\pi i/5}$, $z_5^0 = r_0 e^{6\pi i/5}$, and $z_6^0 = r_0 e^{8\pi i/5}$. (b) The fixed points (highlighted by solid dots) are placed at $z_2^0 = 0$, $z_3^0 = r_0 e^{2\pi i/5}$, $z_4^0 = r_0 e^{4\pi i/5}$, $z_5^0 = r_0 e^{6\pi i/5}$, and $z_6^0 = r_0 e^{8\pi i/5}$, $r_0 = 1.6\ \Lambda$. The units of the vertical axes are arbitrary, but the same for both frames. The same surface portrays also the associated momentum correlations ${}^6\mathcal{G}(k_x, k_y)$, with corresponding mappings for the fixed points, i.e., $r_0 \to k_r^0 = 1.6\ 1/\Lambda$.

whereas in Fig. 11(b), one of the five fixed points was moved from the corner of the pentagon to the origin. In Fig. 11(a), it is apparent that the sixth fermion lies at the origin, while in Fig. 11(b), the sixth fermion completes the apices of the regular pentagon. The above results for the sixth-order correlation function clearly portray the formation of a concentric (1,5) arrangement of the emergent UC-RWM in the LLL in the case of six trapped fermionc atoms, described by the wave function in Eq. (52).

We note that the (1,5) ring geometrical structure found here to be associated with $N = 6$ LLL fermions (both contact interacting and noninteracting) is familiar [31], as one of two competing configurations from the case of $N = 6$ Coulomb-interacting confined electrons in the field of 2D semiconductor quantum dots, the other configuration being a (0,6) arrangement.

VII. DISCUSSION: THE ROLE OF THE WIGNER PARAMETER

The dimensionless parameter R_δ [defined in Eq. (3)] enters naturally in the many-body LLL Hamiltonian in Eq. (2). This applies also for the many-body Hamiltonians for ultracold atoms in nonrotating traps, i.e., when $\Omega = 0$; see, e.g., Ref. [57]. We note that, in the absence of a magnetic field and for a finite number of N trapped electrons in 2D semiconductor quantum dots, a corresponding parameter [31,55,56] (usually referred to as the Wigner parameter) is defined as

$$R_W = Q/(\hbar\omega), \tag{55}$$

where $Q = e^2/(\kappa l_0)$ is the Coulomb repulsive energy between two electrons at a distance equal to the oscillator strength $l_0 = \sqrt{\hbar/(m_e^*\omega)}$, κ is the dielectric constant of the semiconducting medium, m_e^* is the effective mass of the electron, and ω is the frequency of the parabolic (harmonic) 2D potential confinement.

In the case of a high applied magnetic field B (LLL Hilbert space), l_0 in Eq. (55) is replaced by the magnetic length and ω is replaced by the cyclotron frequency, that is, $l_0 \to l_B$ and $\omega \to \omega_c = eB/(m^*c)$, with $l_B = \sqrt{\hbar/(m^*\omega_c)}$. As is the case with the contact interaction, i.e., the fact (discussed in Sec. III) that the LLL spectrum associated solely with the interaction term $H_{\rm int}$ [third term in Eq. (2)] scales with R_δ, the LLL spectrum associated solely with the long-range Coulomb repulsion scales also with R_W. As a result, the values R_δ and R_W do not influence the intrinsic structure of the LLL many-body wave functions. [Note that the eigenstates of $H_{\rm int}$ are also eigenstates of the LLL kinetic-energy Hamiltonian H_K; see second term in Eq. (2)]. The independence of WM formation from the precise value of R_δ is further demonstrated in Fig. 12 in Appendix C, where a different value $R_\delta = 0.2$ was used.

The only effect of the magnitude of R_δ is to determine the precise value of Ω/ω where the crossings in Fig. 1 occur. In contrast, for vanishing and small magnetic fields, or for a nonrotating trap, the emergence of the Wigner molecular structures does depend on the value of R_W and R_δ, respectively, requiring values of these parameters larger than unity [23–25,31,55–58,86].

The apparent above inconsistency concerning the qualitative role of the Wigner parameter motivates the following deeper insight. Indeed, both the R_W and R_δ parameters at $B = 0$ and $\Omega = 0$, respectively, express the ratio

$$\mathcal{R} = \frac{\Delta E_{\rm int}}{\Delta E_{\rm sp}}, \tag{56}$$

where $\Delta E_{\rm int}$ is a representative amount of repulsive energy and $\Delta E_{\rm sp}$ is an average energy spacing in the single-particle spectrum. For $B = 0$, or $\Omega = 0$, the $\hbar\omega$ used in Eqs. (3) and (55) reflects indeed the average energy gap between the single-particle states of the familiar 2D harmonic oscillator. In the case of the Landau-level spectrum (Fock-Darwin oscillator [31,35,36]), $2\hbar\omega$, or $\hbar\omega_c$, represents the energy spacing between Landau levels. However, the relevant many-body Hilbert space is restricted in the LLL where the energy gap

between the single-particle states vanishes due to the well-known infinite degeneracy of the Landau levels; this is also referred to as single-particle kinetic-energy quenching. Thus, with respect to the pertinent dimensionless parameter that controls Wigner-molecule formation in the LLL, the denominator in Eq. (56) must be taken to be precisely zero, which results in all instances in an infinite value for $\mathcal{R}$. Interestingly, the single-outcome value of $R \to +\infty$ implies that the LLL many-body case is preset for favoring the emergence of Wigner molecules, independently of the strength or the type of the two-body interaction. In fact, in addition to the Coulombic and contact-interaction cases, this qualitative prediction has been confirmed by numerical calculations in the case of few fully spin-polarized LLL fermions interacting via a dipole-dipole potential [87].

VIII. SUMMARY

The development and employment of both computational, numerical (two-dimensional configuration interaction [21,22,31]), and algebraic (MATHEMATICA [73]) state-of-the-art methodological approaches were shown here to bring forth advanced tools (e.g., all-order momentum correlations) that boost and refine our ability to in-depth interrogate the complex many-body physics underlying the fractional quantum-Hall effect in assemblies of a few ultracold neutral fermionic atoms, interacting via repulsive contact potentials and confined in a single rapidly rotating two-dimensional harmonic trap. We considered spinful fermionic atom assemblies, where in addition to the two-dimensional orbital degree of freedom, each orbital within a degenerate Landau level state has also spin degrees of freedom. Detailed results were given for the illustrative example of four spinful ultracold fermions in a rapidly rotating trap (a case anticipated to be among the first to be experimentally explored in the near future).

As pointed out earlier [9,13,14,20], rotating assemblies of a few ultracold atoms have become particularly promising for exploring the LLL physics due to experimental difficulties in reaching sufficiently dilute regimes (low filling fractions) with a large number of atoms [88,89] in rotating traps; in the former experiment [88] high rotational rates of a BEC cloud of ^{87}Rb atoms resulted in formation of ordered Abrikosov vortices, and similarly for the case of a large-number BEC cloud of ^{7}Li atoms [89]. In this context, the raised level of understanding brought forth by consideration of the N-body correlations, compared to studies limited to examination of merely the 2nd-order ones, appears to be pivotal for making further progress in this field. This is the case in particular because the experimental window of fermionic LLL states is restricted to the lowest range of total angular momenta, up to values in the neighborhood of $L_{(1,1,1)}$ associated with the (1,1,1) Halperin wave function. Indeed for spin-balanced assemblies (with N particles), the total angular momentum value is $L_{(1,1,1)} = N(N-1)/2$, which is smaller than the value of $N(N-1)$ for the bosonic, and $3N(N-1)/2$ for the fermionic, Laughlin states.

Our analysis showed that the few-body LLL states with magic angular momenta exhibit intrinsic ordered quantum structures in the N-body correlations, similar to those associated with rotating Wigner molecules [21,31], familiar from the field of semiconductor quantum dots under high magnetic fields.

The application of a small perturbing stirring potential V_p [specifically a multipole deformation of the trap; see Eq. (6)] induces, in the neighborhood of the ensuing avoided crossings in the global LLL energy spectra [see Fig. 1 associated with the $(S=0,\ S_z=0)$ spin sector], states with broken rotational symmetry (i.e., without good total angular momenta, referred to accordingly as pinned Wigner molecules). These structures exhibit molecular-type (or crystalline-type) configurations which are manifested already at the lowest level of first-order correlations (i.e., in the single-particle CI spin-unresolved densities; see Fig. 5). This behavior portrays characteristics reminiscent of the "flea on the elephant" concept [69–71], familiar from the mathematical treatment of spontaneous symmetry-breaking phenomena [72].

Furthermore, our analysis identified a CI LLL state in the $(S=2,\ S_z=0)$ spin sector, which was shown to be well described by a Halperin (1,1,1) two-component orbital variational wave function. Analysis of this CI LLL wave function enabled a two-dimensional generalization of the Girardeau one-dimensional "fermionization" scheme [34], originally invoked for the mapping of bosonic-type wave functions to those of spinless fermions.

We stress that our systematic comparative analysis and investigations led us to conclude that in order to uncover the intrinsic geometrical structural characteristics of the symmetry-preserving ultracold rotating Wigner molecules that form in the rotating traps and exhibit magic angular momenta, it is imperative to carry out analysis that goes beyond second-order correlations in the real configuration space. To assist the design and analysis of experimental observations in 2D traps, we illustrate these findings through benchmark theoretical predictions for all-order spin-unresolved, as well as spin-resolved, all-order momentum correlations. These can be indeed directly measured [17,18,90] with time-of-flight protocols employing individual particle detection in the far-field region.

Our conclusions regarding all-order momentum correlations apply to the correlated FQHE states formed in ultracold neutral atom assemblies trapped in rotating traps on which we focused in this study, as well as to future investigations, including interrogations of quantum magnetism in finite 2D systems (extending previous studies on 1D trapped ultracold atoms [74,91]), hole pairing in 2D plaquettes [92], and Mott insulator to superfluid quantum phase transitions in finite 2D ultracold atom systems [93].

ACKNOWLEDGMENTS

This work has been supported by a grant from the Air Force Office of Scientific Research (AFOSR, USA) under Award No. FA9550-15-1-0519. Calculations were carried out at the GATECH Center for Computational Materials Science.

APPENDIX A: MAGIC ANGULAR MOMENTA FOR THE $N = 3$ WM WITH SPINFUL FERMIONS

To enhance the brief historical overview in Sec. III, and to illustrate the role of the underlying geometric picture, we

sketch here the derivation for the spin-dependent magic angular momenta in the simpler case of three localized fermions arranged in an intrinsic configuration of an equilateral triangle [94]. For $N = 3$ fermions, both the $S_z = \frac{1}{2}$ and $\frac{3}{2}$ polarizations need to be considered. We start with the $S_z = \frac{1}{2}$ polarization, which is associated with three spin primitives $|\downarrow\uparrow\uparrow\rangle$, $|\uparrow\downarrow\uparrow\rangle$, and $|\uparrow\uparrow\downarrow\rangle$. These primitives correspond to single Slater determinants which exhibit a breaking of both the total spin symmetry and of the continuous rotational symmetry. We first proceed with the restoration of the total spin by noticing that the three spin primitives have a point-group symmetry lower than the C_3 symmetry of an equilateral triangle. The C_3 symmetry, however, can be readily restored by applying appropriate point-group projection operators according to group-theoretical concepts [95,96]. This yields the following two different three-determinantal combinations for the intrinsic part of the many-body wave function:

$$\Phi_1^{\rm intr}(\gamma_0) = |\downarrow\uparrow\uparrow\rangle + e^{2\pi i/3}|\uparrow\downarrow\uparrow\rangle + e^{-2\pi i/3}|\uparrow\uparrow\downarrow\rangle \quad \text{(A1)}$$

and

$$\Phi_2^{\rm intr}(\gamma_0) = |\downarrow\uparrow\uparrow\rangle + e^{-2\pi i/3}|\uparrow\downarrow\uparrow\rangle + e^{2\pi i/3}|\uparrow\uparrow\downarrow\rangle. \quad \text{(A2)}$$

Here, $\gamma_0 = 0$ denotes the azimuthal angle of the triangle vertex associated with the position of the original spin-down fermion in $|\downarrow\uparrow\uparrow\rangle$. We note that the intrinsic wave functions $\Phi_1^{\rm intr}$ and $\Phi_2^{\rm intr}$ are eigenstates of the square of the total spin operator $\hat{\mathbf{S}}^2$ ($\hat{\mathbf{S}} = \sum_{i=1}^3 \hat{\mathbf{s}}_i$) with quantum number $S = \frac{1}{2}$. This can be verified directly by applying to them the $\hat{\mathbf{S}}^2$ as given in Eq. (15).

To restore the circular symmetry, one applies the continuous space projection operator [31]

$$2\pi \mathcal{P}_L \equiv \int_0^{2\pi} d\gamma \, \exp[-i\gamma(\hat{L} - L)] \,, \quad \text{(A3)}$$

where $\hat{L} = \sum_{j=1}^N \hat{l}_j$ is the operator for the total angular momentum.

The resulting wave function Ξ has both good total spin and angular momentum quantum numbers; it is of the form

$$2\pi\,\Xi = \int_0^{2\pi} d\gamma \, \Phi_{\rm 1or2}^{\rm intr}(\gamma) e^{i\gamma L}, \quad \text{(A4)}$$

where now the intrinsic wave function [given by Eq. (A1) or (A2)] has an arbitrary azimuthal orientation γ, which is integrated out.

The operator $\hat{R}(2\pi/3) \equiv \exp(-i2\pi\hat{L}/3)$ can be applied to Ξ in two different ways, namely, either on the intrinsic part $\Phi^{\rm intr}$ or the external part $\exp(i\gamma L)$. Using Eq. (A1) and the property $\hat{R}(2\pi/3)\Phi_1^{\rm intr} = \exp(-2\pi i/3)\Phi_1^{\rm intr}$, one finds

$$\hat{R}(2\pi/3)\Xi = \exp(-2\pi i/3)\Xi \quad \text{(A5)}$$

from the first alternative, and

$$\hat{R}(2\pi/3)\Xi = \exp(-2\pi Li/3)\Xi \quad \text{(A6)}$$

from the second alternative. Now, if $\Xi \neq 0$, the only way that Eqs. (A5) and (A6) can be simultaneously true is if the condition $\exp[2\pi(L-1)i/3] = 1$ is fulfilled. This leads to a first sequence of magic angular momenta associated with total spin $S = \frac{1}{2}$, i.e.,

$$L = 3n + 1, \;\; n = 0, \pm1, \pm2, \pm3, \ldots . \quad \text{(A7)}$$

Using Eq. (A2) for the intrinsic wave function, and following similar steps, one can derive a second sequence of magic angular momenta associated with good total spin $S = \frac{1}{2}$, i.e.,

$$L = 3n - 1, \;\; n = 0, \pm1, \pm2, \pm3, \ldots . \quad \text{(A8)}$$

In the fully polarized case, the spin primitive $|\uparrow\uparrow\uparrow\rangle$ is already an eigenstate of $\hat{\mathbf{S}}^2$ with quantum number $S = \frac{3}{2}$. Thus, only the rotational symmetry needs to be restored, that is, the intrinsic wave function is simply $\Phi_3^{\rm intr}(\gamma_0) = |\uparrow\uparrow\uparrow\rangle$. Since $\hat{R}(2\pi/3)\Phi_3^{\rm intr} = \Phi_3^{\rm intr}$, the condition for the allowed angular momenta is $\exp[-2\pi Li/3] = 1$, which yields the following magic angular momenta:

$$L = 3n, \;\; n = 0, \pm1, \pm2, \pm3, \ldots . \quad \text{(A9)}$$

We mention again here that only non-negative angular momenta are present in the LLL.

APPENDIX B: THE 20 SPIN PRIMITIVES FOR $N = 6$ FERMIONS

The 20 spin primitives for $N = 6$ fermions are as follows:

$$Z_1 = \alpha(1)\alpha(2)\alpha(3)\beta(4)\beta(5)\beta(6),$$
$$Z_2 = \alpha(1)\alpha(2)\alpha(4)\beta(3)\beta(5)\beta(6),$$
$$Z_3 = \alpha(1)\alpha(2)\alpha(5)\beta(3)\beta(4)\beta(6),$$
$$Z_4 = \alpha(1)\alpha(2)\alpha(6)\beta(3)\beta(4)\beta(5),$$
$$Z_5 = \alpha(1)\alpha(3)\alpha(4)\beta(2)\beta(5)\beta(6),$$

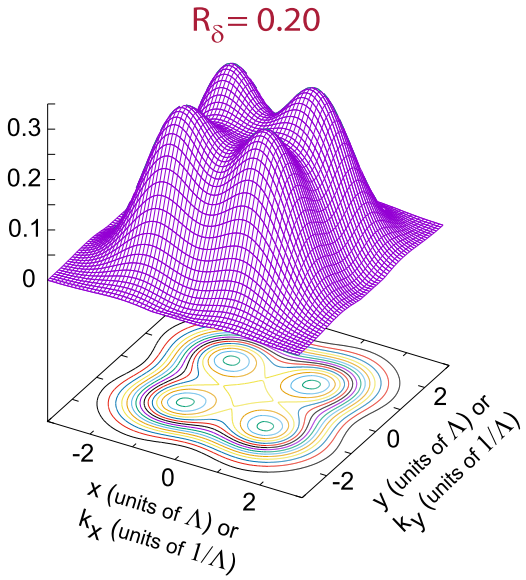

FIG. 12. CI single-particle density (both in real space and momentum space) of the relative ground state of $N = 4$ fermions in the spin sector with ($S = 0$, $S_z = 0$), but considering $R_\delta = 0.20$, in contrast to the value $R_\delta = 0.40$ used in the calculations in the main text. 3D surfaces are plotted. $\mathcal{C} = 0.004$ at the point $\Omega/\omega = 0.9445$ (situated at the avoided crossing between $L = 4$ and 8). The expectation value of the total angular momentum is $\langle L\rangle = 7.8739$, indicating that the plotted case is a state with broken rotational symmetry. For the spatial density, the vertical axis is in units of $1/\Lambda^2$. For the momentum density, the vertical axis is in units of Λ^2.

$$
\begin{aligned}
Z_6 &= \alpha(1)\alpha(3)\alpha(5)\beta(2)\beta(4)\beta(6),\\
Z_7 &= \alpha(1)\alpha(3)\alpha(6)\beta(2)\beta(4)\beta(5),\\
Z_8 &= \alpha(1)\alpha(4)\alpha(5)\beta(2)\beta(3)\beta(6),\\
Z_9 &= \alpha(1)\alpha(4)\alpha(6)\beta(2)\beta(3)\beta(5),\\
Z_{10} &= \alpha(1)\alpha(5)\alpha(6)\beta(2)\beta(3)\beta(4),\\
Z_{11} &= \alpha(2)\alpha(3)\alpha(4)\beta(1)\beta(5)\beta(6),\\
Z_{12} &= \alpha(2)\alpha(3)\alpha(5)\beta(1)\beta(4)\beta(6),\\
Z_{13} &= \alpha(2)\alpha(3)\alpha(6)\beta(1)\beta(4)\beta(5),\\
Z_{14} &= \alpha(2)\alpha(4)\alpha(5)\beta(1)\beta(3)\beta(6),\\
Z_{15} &= \alpha(2)\alpha(4)\alpha(6)\beta(1)\beta(3)\beta(5),\\
Z_{16} &= \alpha(2)\alpha(5)\alpha(6)\beta(1)\beta(3)\beta(4),\\
Z_{17} &= \alpha(3)\alpha(4)\alpha(5)\beta(1)\beta(2)\beta(6),\\
Z_{18} &= \alpha(3)\alpha(4)\alpha(6)\beta(1)\beta(2)\beta(5),\\
Z_{19} &= \alpha(3)\alpha(5)\alpha(6)\beta(1)\beta(2)\beta(4),\\
Z_{20} &= \alpha(4)\alpha(5)\alpha(6)\beta(1)\beta(2)\beta(3). \qquad \text{(B1)}
\end{aligned}
$$

APPENDIX C: A CI CALCULATION FOR $N = 4$ LLL FERMIONS AND $R_\delta = 0.20$

An example of the formation of a pinned WM for a different value of R_δ, i.e., $R_\delta = 0.20$, is given with Fig. 12.

[1] D. C. Tsui, H. L. Stormer, and A. C. Gossard, Two-Dimensional Magnetotransport in the Extreme Quantum Limit, Phys. Rev. Lett. **48**, 1559 (1982).

[2] R. B. Laughlin, Quantized motion of three two-dimensional electrons in a strong magnetic field, Phys. Rev. B **27**, 3383 (1983).

[3] R. B. Laughlin, Anomalous Quantum Hall Effect: An Incompressible Quantum Fluid with Fractionally Charged Excitations, Phys. Rev. Lett. **50**, 1395 (1983).

[4] B. I. Halperin, Theory of the Quantized Hall Conductance, Helv. Phys. Acta **56**, 75 (1983).

[5] J. K. Jain, Composite-Fermion Approach for the Fractional Quantum Hall Effect, Phys. Rev. Lett. **63**, 199 (1989).

[6] C. Yannouleas and U. Landman, Trial wave functions with long-range Coulomb correlations for two-dimensional N-electron systems in high magnetic fields, Phys. Rev. B **66**, 115315 (2002).

[7] N. K. Wilkin and J. M. F. Gunn, Condensation of "Composite Bosons" in a Rotating BEC, Phys. Rev. Lett. **84**, 6 (2000).

[8] N. Read and N. R. Cooper, Free expansion of lowest-Landau-level states of trapped atoms: A wave-function microscope, Phys. Rev. A **68**, 035601 (2003).

[9] M. Popp, B. Paredes, and J. I. Cirac, Adiabatic path to fractional quantum Hall states of a few bosonic atoms, Phys. Rev. A **70**, 053612 (2004).

[10] N. Barberán, M. Lewenstein, K. Osterloh, and D. Dagnino, Ordered structures in rotating ultracold Bose gases, Phys. Rev. A **73**, 063623 (2006).

[11] L. O. Baksmaty, C. Yannouleas, and U. Landman, Rapidly rotating boson molecules with long- or short-range repulsion: An exact diagonalization study, Phys. Rev. A **75**, 023620 (2007).

[12] N. R. Cooper, Rapidly rotating atomic gases, Adv. Phys. **57**, 539 (2008).

[13] S. K. Baur, K. R. A. Hazzard, and E. J. Mueller, Stirring trapped atoms into fractional quantum Hall puddles, Phys. Rev. A **78**, 061608(R) (2008).

[14] N. Gemelke, E. Sarajlic, and S. Chu, Rotating few-body atomic systems in the fractional quantum hall regime, arXiv:1007.2677.

[15] F. Serwane, G. Zürn, T. Lompe, T. B. Ottenstein, A. N. Wenz, and S. Jochim, Deterministic preparation of a tunable few-fermion system, Science **332**, 336 (2011).

[16] G. Zürn, F. Serwane, T. Lompe, A. N. Wenz, M. G. Ries, J. E. Bohn, and S. Jochim, Fermionization of Two Distinguishable Fermions, Phys. Rev. Lett. **108**, 075303 (2012).

[17] A. Bergschneider, V. M. Klinkhamer, J. H. Becher, R. Klemt, L. Palm, G. Zürn, S. Jochim, and P. M. Preiss, Experimental characterization of two-particle entanglement through position and momentum correlations, Nat. Phys. **15**, 640 (2019).

[18] P. M. Preiss, J. H. Becher, R. Klemt, V. Klinkhamer, A. Bergschneider, N. Defenu, and S. Jochim, High-Contrast Interference of Ultracold Fermions, Phys. Rev. Lett. **122**, 143602 (2019).

[19] J. H. Becher, E. Sindici, R. Klemt, S. Jochim, A. J. Daley, and P. M. Preiss, Measurement of identical particle entanglement and the influence of antisymmetrisation, arXiv:2002.11207.

[20] L. Palm, *Exploring Fractional Quantum Hall Physics Using Ultracold Fermions in Rotating Traps*, Master thesis, Heidelberg, 2018; see also R.-J. Petzold, *Few Ultracold Fermions in a Two-Dimensional Trap*, Master thesis, Heidelberg, 2020.

[21] C. Yannouleas and U. Landman, Two-dimensional quantum dots in high magnetic fields: Rotating-electron-molecule versus composite-fermion approach, Phys. Rev. B **68**, 035326 (2003).

[22] C. Yannouleas and U. Landman, Structural properties of electrons in quantum dots in high magnetic fields: Crystalline character of cusp states and excitation spectra, Phys. Rev. B **70**, 235319 (2004).

[23] M. Rontani, C. Cavazzoni, D. Bellucci, and G. Goldoni, Full configuration interaction approach to the few-electron problem in artificial atoms, J. Chem. Phys. **124**, 124102 (2006).

[24] Y. Li, C. Yannouleas, and U. Landman, Three-electron anisotropic quantum dots in variable magnetic fields: Exact results for excitation spectra, spin structures, and entanglement, Phys. Rev. B **76**, 245310 (2007); **81**, 049902(E) (2010).

[25] S. A. Blundell and S. Chacko, Isomeric and hybrid isomeric-vibrational states of Wigner molecules, Phys. Rev. B **81**, 121104(R) (2010).

[26] A. Szabo and N. S. Ostlund, *Modern Quantum Chemistry: Introduction to Advanced Electronic Structure Theory*, revised 1st ed. (McGraw-Hill, New York, 1989).

[27] C. Yannouleas and U. Landman, Unified microscopic approach to the interplay of pinned-Wigner-solid and liquid behavior of the lowest Landau-level states in the neighborhood of $\nu = 1/3$, Phys. Rev. B **84**, 165327 (2011).

[28] A. Bergschneider, V. M. Klinkhamer, J. H. Becher, R. Klemt, G. Zürn, P. M. Preiss, and S. Jochim, Spin-resolved single-atom imaging of ^{6}Li in free space, Phys. Rev. A **97**, 063613 (2018).

[29] S. M. Girvin and T. Jach, Interacting electrons in two-dimensional Landau levels: Results for small clusters, Phys. Rev. B **28**, 4506 (1983).

[30] P. A. Maksym and T. Chakraborty, Quantum Dots in a Magnetic Field: Role of Electron-Electron Interactions, Phys. Rev. Lett. **65**, 108 (1990).

[31] C. Yannouleas and U. Landman, Symmetry breaking and quantum correlations in finite systems: studies of quantum dots and ultracold Bose gases and related nuclear and chemical methods, Rep. Prog. Phys. **70**, 2067 (2007).

[32] P. A. Maksym, Eckardt frame theory of interacting electrons in quantum dots, Phys. Rev. B **53**, 10871 (1996).

[33] I. Romanovsky, C. Yannouleas, and U. Landman, Edge states in graphene quantum dots: Fractional quantum Hall effect analogies and differences at zero magnetic field, Phys. Rev. B **79**, 075311 (2009).

[34] M. Girardeau, Relationship between systems of impenetrable bosons and fermions in one dimension, J. Math. Phys. **1**, 516 (1960).

[35] V. Fock, Bemerkung zur Quantelung des harmonischen Oszillators im Magnetfeld, Z. Phys. **47**, 446 (1928).

[36] C. G. Darwin, The Diamagnetism of the Free Electron, C. G. Darwin, Proc. Cambridge Philos. Soc. **27**, 86 (1931)

[37] For details regarding the equivalence between applied magnetic field B and the rotational frequency Ω, as well as the derivation of the spectrum in Eq. (1) (see the Appendix in Ref. [31]; see also Refs. [7,12]).

[38] For an instance of a detailed derivation of $H_{\rm LLL}$, see Sec. II A of Ref. [11].

[39] D. S. Petrov, M. Holzmann, and G. V. Shlyapnikov, Bose-Einstein Condensation in Quasi-2D Trapped Gases, Phys. Rev. Lett. **84**, 2551 (2000).

[40] Concerning earlier literature, R_δ agrees with the parameter η in Ref. [9]. Furthermore, the parameter U in Ref. [13] relates to R_δ as $U = R_\delta \hbar\omega$.

[41] G. E. Astrakharchik, Quantum Monte Carlo study of ultracold gases, Ph.D. dissertation, University of Trento, 2004.

[42] G. Zürn, Few-fermion systems in one dimension, Ph.D. thesis, Heidelberg, 2012.

[43] P. S. Julienne and J. M. Hutson, Contrasting the wide Feshbach resonances in ^{6}Li and ^{7}Li, Phys. Rev. A **89**, 052715 (2014).

[44] For a CI calculation with a different value, i.e., $R_\delta = 0.2$, which illustrates explicitly that the formation of the WMs in the LLL is independent of R_δ, see Fig. 12 in Appendix C.

[45] R. B. Lehoucq, D. C. Sorensen, and C. Yang, *ARPACK Users' Guide: Solution of Large-Scale Eigenvalue Problems with Implicitly Restarted Arnoldi Methods* (SIAM, Philadelphia, 1998).

[46] W. E. Arnoldi, The principle of minimized iterations in the solution of the matrix eigenvalue problem, Q. Appl. Math. **9**, 17 (1951).

[47] G. F. Bertsch and Th. Papenbrock, Yrast Line for Weakly Interacting Trapped Bosons, Phys. Rev. Lett. **83**, 5412 (1999).

[48] See Tables 2.3 and 2.4 on p. 70 of Ref. [26].

[49] E. Altman, E. Demler, and M. D. Lukin, Probing many-body states of ultracold atoms via noise correlations, Phys. Rev. A **70**, 013603 (2004).

[50] W. Y. Ruan, Y. Y. Liu, C. G. Bao, and Z. Q. Zhang, Origin of magic angular momenta in few-electron quantum dots, Phys. Rev. B **51**, 7942(R) (1995).

[51] T. Seki, Y. Kuramoto, and T. Nishino, Origin of magic angular momentum in a quantum dot under strong magnetic field, J. Phys. Soc. Jpn. **65**, 3945 (1996).

[52] C. Yannouleas and U. Landman, Group theoretical analysis of symmetry breaking in two-dimensional quantum dots, Phys. Rev. B **68**, 035325 (2003).

[53] Z. Dai, J.-L. Zhu, N. Yang, and Y. Wang, Spin-dependent rotating Wigner molecules in quantum dots, Phys. Rev. B **76**, 085308 (2007).

[54] C. Shi, G. S. Jeon, and J. K. Jain, Composite fermion solid and liquid states in two component quantum dots, Phys. Rev. B **75**, 165302 (2007).

[55] See the case of two electrons in a 2D parabolic trap, C. Yannouleas and U. Landman, Collective and Independent-Particle Motion in Two-Electron Artificial Atoms, Phys. Rev. Lett. **85**, 1726 (2000).

[56] C. Yannouleas and U. Landman, Spontaneous Symmetry Breaking in Single and Molecular Quantum Dots, Phys. Rev. Lett. **82**, 5325 (1999) Erratum: Spontaneous Symmetry Breaking in Single and Molecular Quantum Dots [Phys. Rev. Lett. **82**, 5325 (1999)], **85**, 2220 (2000).

[57] I. Romanovsky, C. Yannouleas, and U. Landman, Crystalline Boson Phases in Harmonic Traps: Beyond the Gross-Pitaevskii Mean Field, Phys. Rev. Lett. **93**, 230405 (2004).

[58] U. De Giovannini, F. Cavaliere, R. Cenni, M. Sassetti, and B. Kramer, Spin and rotational symmetries in unrestricted Hartree-Fock states of quantum dots, New J. Phys. **9**, 93 (2007).

[59] For the use of this term in the context of electrons in 2D semiconductor quantum dots, see Ref. [31]. The variants of "rotating electron molecule" [31] or "rotating boson molecule" [11] in the case of bosons have also been employed.

[60] C. Ellenberger, T. Ihn, C. Yannouleas, U. Landman, K. Ensslin, D. Driscoll, and A. C. Gossard, Excitation Spectrum of Two Correlated Electrons in a Lateral Quantum Dot with Negligible Zeeman Splitting, Phys. Rev. Lett. **96**, 126806 (2006).

[61] Y. Nishi, P. A. Maksym, D. G. Austin, T. Hatano, L. P. Kouwenhoven, H. Aoki, and S. Tarucha, Intermediate low spin states in a few-electron quantum dot in the $\nu \leqslant 1$ regime, Phys. Rev. B **74**, 033306 (2006).

[62] S. Kalliakos, M. Rontani, V. Pellegrini, C. P. García, A. Pinczuk, G. Goldoni, E. Molinari, L. N. Pfeiffer, and K. W. West, A molecular state of correlated electrons in a quantum dot, Nat. Phys. **4**, 467 (2008).

[63] A. M. Mintairov, J. Kapaldo, J. L. Merz, S. Rouvimov, D. V. Lebedev, N. A. Kalyuzhnyy, S. A. Mintairov, K. G. Belyaev, M. V. Rakhlin, A. A. Toropov *et al.*, Control of Wigner localization and electron cavity effects in near-field emission spectra of In(Ga)P/GaInP quantum-dot structures, Phys. Rev. B **97**, 195443 (2018).

[64] S. Pecker, F. Kuemmeth, A. Secchi, M. Rontani, D. C. Ralph, P. L. McEuen, and S. Ilani, Observation and spectroscopy of

a two-electron Wigner molecule in an ultraclean carbon nanotube, Nat. Phys. **9**, 576 (2013).

[65] G. Hönig, G. Callsen, A. Schliwa, S. Kalinowski, Ch. Kindel, S. Kako, Y. Arakawa, D. Bimberg, and A. Hoffmann, Manifestation of unconventional biexciton states in quantum dots, Nat. Commun. **5**, 5721 (2014).

[66] The (1, 5) ring configuration for $N = 6$ fermions is demonstrated in Sec. VI B.

[67] J. K. Jain, *Composite Fermions* (Cambridge University Press, Cambridge, 2007).

[68] See Supplemental Material at http://link.aps.org/supplemental/10.1103/PhysRevA.102.043317 for (I) additional Tables related to Figs. 5(a-f) and (II) MATHEMATICA scripts related to Sections IV D, V B, VI A, and VI B.

[69] Ch. J. F. van de Ven, C. Gerrit, R. R. Groenenboom, and N. P. Landsman, Quantum spin systems versus Schrödinger operators: A case study in spontaneous symmetry breaking, SciPost Phys. **8**, 022 (2020).

[70] G. Jona-Lasinio, F. Martinelli, and E. Scoppola, New approach to the semiclassical limit of quantum mechanics, Commun. Math. Phys. **80**, 223 (1981).

[71] B. Simon, Semiclassical analysis of low lying eigenvalues. IV. The flea on the elephant, J. Funct. Anal. **63**, 123 (1985).

[72] P. W. Anderson, An approximate quantum theory of the antiferromagnetic ground state, Phys. Rev. **86**, 694 (1952).

[73] Wolfram Research, Inc., MATHEMATICA, Version 12.1, Champaign, IL (2020).

[74] C. Yannouleas, B. B. Brandt, and U. Landman, Ultracold few fermionic atoms in needle-shaped double wells: spin chains and resonating spin clusters from microscopic Hamiltonians emulated via antiferromagnetic Heisenberg and t-J models, New J. Phys. **18**, 073018 (2016).

[75] A. H. MacDonald, H. A. Fertig, and L. Brey, Skyrmions without Sigma Models in Quantum Hall Ferromagnets, Phys. Rev. Lett. **76**, 2153 (1996).

[76] S. M. Girvin and A. H. MacDonald, Multicomponent Quantum Hall Systems: The Sum of Their Parts and More, in *Perspectives in Quantum Hall Effects: Novel Quantum Liquids in Low-Dimensional Semiconductor Structures*, edited by S. Das Sarma and A. Pinczuk (Wiley, Weinheim, 1996).

[77] D. Tong, Lectures on the Quantum Hall Effect, arXiv:1606.06687v2.

[78] The corresponding filling factor is $\nu = 2/(p+q)$, i.e., $\nu = 1$ for $p = q = 1$.

[79] It turns out that this state becomes also the global ground state in all spin sectors for $\Omega/\omega \gtrsim 0.77$.

[80] R. A. Smith and N. K. Wilkin, Exact eigenstates for repulsive bosons in two dimensions, Phys. Rev. A **62**, 061602(R) (2000).

[81] Th. Papenbrock and G. F. Bertsch, Rotational spectra of weakly interacting Bose-Einstein condensates, Phys. Rev. A **63**, 023616 (2001).

[82] C. Yannouleas and U. Landman, Quantal molecular description and universal aspects of the spectra of bosons and fermions in the lowest Landau level, Phys. Rev. A **81**, 023609 (2010).

[83] G. Moore and N. Read, Nonabelions in the fractional quantum Hall effect, Nucl. Phys. B **360**, 362 (1991).

[84] See Sec. III D and Fig. 4 in Ref. [82].

[85] For a similar effect of the Pauli exclusion principle regarding the formation of a Wigner molecule in the case of $N = 2$ ultracold fermionic atoms confined in a single quasi-1D well, see the comparison of second-order correlations between the singlet and triplet states in Sec. III A of B. B. Brandt, C. Yannouleas, and U. Landman, Two-point momentum correlations of few ultracold quasi-one-dimensional trapped fermions: Diffraction patterns, Phys. Rev. A **96**, 053632 (2017); compare also Fig. 2(e) (singlet) and Fig. 2(g) (triplet) in Double-well ultracold-fermions computational microscopy: Wave-function anatomy of attractive-pairing and Wigner-molecule entanglement and natural orbitals, Nano Lett. **15**, 7105 (2015); Naturally, unlike the LLL case, a strong repulsion (for separating the particles) is needed for the formation of the singlet-state Wigner molecule in a nonrotating trap. Without addressing the fermionization mapping, the limiting case (referred to as a Pauli crystal) of a Wigner molecule associated with fully polarized ultracold fermions in a static 2D harmonic trap has been discussed in M. Holten, L. Bayha, K. Subramanian, C. Heintze, Ph. M. Preiss, and S. Jochim, Observation of pauli crystals, arXiv:2005.03929; and in M. Gajda, J. Mostowski, T. Sowiński, and M. Załuska-Kotur, Single-shot imaging of trapped Fermi gas, Europhys. Lett. **115**, 20012 (2016).

[86] A direct visualization of this trend is seen at the mean-field level, where symmetry-broken wave functions are obtained as the value of these parameters increases [56]. Restoration [31,57,58] of the broken rotational and spin symmetries via projection techniques produces symmetry-preserving wave functions that are comparable to the CI many-body ones [31,57,58]; for the simpler case of two electrons, see C. Yannouleas and U. Landman, Strongly correlated wave functions for artificial atoms and molecules, J. Phys.: Condens. Matter **14**, L591 (2002); See also Y. Li, C. Yannouleas, and U. Landman, From a few to many electrons in quantum dots under strong magnetic fields: Properties of rotating electron molecules with multiple rings, Phys. Rev. B **73**, 075301 (2006).

[87] K. Osterloh, N. Barberán, and M. Lewenstein, Strongly Correlated States of Ultracold Rotating Dipolar Fermi Gases, Phys. Rev. Lett. **99**, 160403 (2007).

[88] V. Schweikhard, I. Coddington, P. Engels, V. P. Mogendorff, and E. A. Cornell, Rapidly Rotating Bose-Einstein Condensates in and near the Lowest Landau Level, Phys. Rev. Lett. **92**, 040404 (2004).

[89] M. W. Zwierlein, J. R. Abo-Shaeer, A. Schirotzek, C. H. Schunck, and W. Ketterle, Vortices and superfluidity in a strongly interacting Fermi gas, Nature (London) **435**, 1047 (2005).

[90] C. Carcy, H. Cayla, A. Tenart, A. Aspect, M. Mancini, and D. Clément, Momentum-Space Atom Correlations in a Mott Insulator, Phys. Rev. X **9**, 041028 (2019).

[91] S. Murmann, F. Deuretzbacher, G. Zürn, J. Bjerlin, S. M. Reimann, L. Santos, T. Lompe, and S. Jochim, Antiferromagnetic Heisenberg Spin Chain of a Few Cold Atoms in a One-Dimensional Trap, Phys. Rev. Lett. **115**, 215301 (2015).

[92] B. B. Brandt, C. Yannouleas, and U. Landman, Bottom-up configuration-interaction emulations of ultracold fermions in entangled and tunnel-coupled two-dimensional optical plaquettes: Building blocks of unconventional superconductivity, Phys. Rev. A **95**, 043617 (2017).

[93] C. Yannouleas and U. Landman, All-order momentum correlations of three ultracold bosonic atoms confined in triple-well traps: Signatures of emergent many-body quantum phase transitions and analogies with three-photon quantum-optics interference, Phys. Rev. A **101**, 063614 (2020).

[94] For details, especially concerning the group-theoretical aspects, see Ref. [52].

[95] F. A. Cotton, *Chemical Applications of Group Theory* (Wiley, New York, 1990).

[96] A. B. Wolbarst, *Symmetry and Quantum Systems* (Van Nostrand Reinold, New York, 1977).

SUPPLEMENTAL MATERIAL I

Fractional-quantum-Hall physics and higher-order momentum correlations in few spinful fermionic contact-interacting ultracold atoms in rotating traps

Constantine Yannouleas[†] and Uzi Landman[*]
School of Physics, Georgia Institute of Technology, Atlanta, Georgia 30332-0430

Contents:

[†]Constantine.Yannouleas@physics.gatech.edu
[*]Uzi.Landman@physics.gatech.edu

TABLE STI. Dominant coefficients, $c(I)$, in the CI expansion of the relative LLL ground state (with $\langle L\rangle = 7.189$) in the ($S = 0$, $S_z = 0$) spin sector corresponding to the symmetry-broken state whose single-particle density portrayed in Figs. 5(a,b) of the main text. The CI expansion consists of $I_{\rm total} = 1296$ basis determinants. The index J is introduced to relabel the dominant coefficients, with the dominance criterion being $|c(I)| > 0.01$. 48 determinants with total angular momenta $L = 4$, 8, or 12 participate in this TABLE. Note that $\sum_{i=1}^{48} |c(J)|^2 = 0.99843$, i.e., the corresponding contribution to the normalization constant differs from unity only in the third decimal point.

I	J	$c(J)$	$(l_1\uparrow, l_2\uparrow, l_3\downarrow, l_4\downarrow)$	$\sum_{i=1}^{4} l_i$	I	J	$c(J)$	$(l_1\uparrow, l_2\uparrow, l_3\downarrow, l_4\downarrow)$	$\sum_{i=1}^{4} l_i$
3	1	0.1422510E+00	(0, 1, 0, 3)	4	303	25	-0.1891212E-01	(1, 2, 1, 8)	12
9	2	0.1926172E+00	(0, 1, 1, 2)	4	304	26	0.1504875E+00	(1, 2, 2, 3)	8
13	3	-0.1348374E-01	(0, 1, 1, 6)	8	328	27	-0.1218959E+00	(1, 3, 0, 4)	8
22	4	0.2479879E+00	(0, 1, 3, 4)	8	332	28	0.1086694E-01	(1, 3, 0, 8)	12
26	5	-0.2194019E-01	(0, 1, 3, 8)	12	334	29	-0.3688811E+00	(1, 3, 1, 3)	8
29	6	0.1561250E-01	(0, 1, 4, 7)	12	338	30	0.2314515E-01	(1, 3, 1, 7)	12
38	7	-0.3103776E+00	(0, 2, 0, 2)	4	363	31	0.1260920E+00	(1, 4, 0, 3)	8
42	8	0.1509984E-01	(0, 2, 0, 6)	8	369	32	0.2134452E+00	(1, 4, 1, 2)	8
53	9	-0.3058820E+00	(0, 2, 2, 4)	8	433	33	-0.1348374E-01	(1, 6, 0, 1)	8
57	10	0.2696752E-01	(0, 2, 2, 8)	12	478	34	0.2314515E-01	(1, 7, 1, 3)	12
64	11	-0.1272792E-01	(0, 2, 4, 6)	12	507	35	-0.1107325E-01	(1, 8, 0, 3)	12
73	12	0.1422510E+00	(0, 3, 0, 1)	4	513	36	-0.1891212E-01	(1, 8, 1, 2)	12
83	13	0.1260920E+00	(0, 3, 1, 4)	8	543	37	0.2601536E+00	(2, 3, 0, 3)	8
87	14	-0.1107325E-01	(0, 3, 1, 8)	12	547	38	-0.1633527E-01	(2, 3, 0, 7)	12
88	15	0.2601536E+00	(0, 3, 2, 3)	8	549	39	0.1504875E+00	(2, 3, 1, 2)	8
92	16	-0.1637189E-01	(0, 3, 2, 7)	12	578	40	-0.3058820E+00	(2, 4, 0, 2)	8
96	17	0.1070732E-01	(0, 3, 3, 6)	12	582	41	0.1268128E-01	(2, 4, 0, 6)	12
118	18	-0.1218959E+00	(0, 4, 1, 3)	8	687	42	-0.1637189E-01	(2, 7, 0, 3)	12
182	19	0.1509984E-01	(0, 6, 0, 2)	8	722	43	0.2696752E-01	(2, 8, 0, 2)	12
197	20	0.1268128E-01	(0, 6, 2, 4)	12	757	44	0.2479879E+00	(3, 4, 0, 1)	8
232	21	-0.1633527E-01	(0, 7, 2, 3)	12	831	45	0.1070732E-01	(3, 6, 0, 3)	12
262	22	0.1086694E-01	(0, 8, 1, 3)	12	901	46	-0.2194019E-01	(3, 8, 0, 1)	12
289	23	0.1926172E+00	(1, 2, 0, 1)	4	974	47	-0.1272792E-01	(4, 6, 0, 2)	12
299	24	0.2134452E+00	(1, 2, 1, 4)	8	1009	48	0.1561250E-01	(4, 7, 0, 1)	12

TABLE STII. Dominant coefficients, $c(I)$, in the CI expansion of the relative LLL ground state (with $\langle L\rangle = 8.0364$) in the $(S = 0, S_z = 0)$ spin sector corresponding to the symmetry-broken state whose single-particle density portrayed in Figs. 5(c,d) of the main text. The CI expansion consists of $I_{\rm total} = 1296$ basis determinants. The index J is introduced to relabel the dominant coefficients, with the dominance criterion being $|c(I)| > 0.01$. 54 determinants with total angular momenta $L = 4$, 8, or 12 participate in this TABLE. Note that $\sum_{i=1}^{54} |c(J)|^2 = 0.99912$, i.e., the corresponding contribution to the normalization constant differs from unity only in the fourth decimal point.

I	J	$c(J)$	$(l_1\uparrow, l_2\uparrow, l_3\downarrow, l_4\downarrow)$	$\sum_{i=1}^{4} l_i$	I	J	$c(J)$	$(l_1\uparrow, l_2\uparrow, l_3\downarrow, l_4\downarrow)$	$\sum_{i=1}^{4} l_i$
3	1	-0.2252529E-01	(0, 1, 0, 3)	4	332	28	-0.1409311E-01	(1, 3, 0, 8)	12
9	2	-0.2769987E-01	(0, 1, 1, 2)	4	334	29	0.4149306E+00	(1, 3, 1, 3)	8
22	3	-0.2782560E+00	(0, 1, 3, 4)	8	338	30	-0.2986886E-01	(1, 3, 1, 7)	12
26	4	0.2823010E-01	(0, 1, 3, 8)	12	347	31	0.1136427E-01	(1, 3, 3, 5)	12
29	5	-0.2007129E-01	(0, 1, 4, 7)	12	363	32	-0.1395374E+00	(1, 4, 0, 3)	8
38	6	0.4715954E-01	(0, 2, 0, 2)	4	367	33	0.1005852E-01	(1, 4, 0, 7)	12
53	7	0.3406431E+00	(0, 2, 2, 4)	8	369	34	-0.2401117E+00	(1, 4, 1, 2)	8
57	8	-0.3453988E-01	(0, 2, 2, 8)	12	373	35	0.1136298E-01	(1, 4, 1, 6)	12
64	9	0.1613584E-01	(0, 2, 4, 6)	12	443	36	0.1136298E-01	(1, 6, 1, 4)	12
73	10	-0.2252529E-01	(0, 3, 0, 1)	4	472	37	-0.1001277E-01	(1, 7, 0, 4)	12
83	11	-0.1395374E+00	(0, 3, 1, 4)	8	478	38	-0.2986886E-01	(1, 7, 1, 3)	12
87	12	0.1413700E-01	(0, 3, 1, 8)	12	507	39	0.1413700E-01	(1, 8, 0, 3)	12
88	13	-0.2935452E+00	(0, 3, 2, 3)	8	513	40	0.2436981E-01	(1, 8, 1, 2)	12
92	14	0.2115172E-01	(0, 3, 2, 7)	12	543	41	-0.2935452E+00	(2, 3, 0, 3)	8
96	15	-0.1388384E-01	(0, 3, 3, 6)	12	547	42	0.2112242E-01	(2, 3, 0, 7)	12
118	16	0.1387186E+00	(0, 4, 1, 3)	8	549	43	-0.1691131E+00	(2, 3, 1, 2)	8
122	17	-0.1001277E-01	(0, 4, 1, 7)	12	578	44	0.3406431E+00	(2, 4, 0, 2)	8
197	18	-0.1612048E-01	(0, 6, 2, 4)	12	582	45	-0.1612048E-01	(2, 4, 0, 6)	12
227	19	0.1005852E-01	(0, 7, 1, 4)	12	687	46	0.2115172E-01	(2, 7, 0, 3)	12
232	20	0.2112242E-01	(0, 7, 2, 3)	12	693	47	0.1214360E-01	(2, 7, 1, 2)	12
262	21	-0.1409311E-01	(0, 8, 1, 3)	12	722	48	-0.3453988E-01	(2, 8, 0, 2)	12
289	22	-0.2769987E-01	(1, 2, 0, 1)	4	757	49	-0.2782560E+00	(3, 4, 0, 1)	8
299	23	-0.2401117E+00	(1, 2, 1, 4)	8	802	50	0.1136427E-01	(3, 5, 1, 3)	12
303	24	0.2436981E-01	(1, 2, 1, 8)	12	831	51	-0.1388384E-01	(3, 6, 0, 3)	12
304	25	-0.1691131E+00	(1, 2, 2, 3)	8	901	52	0.2823010E-01	(3, 8, 0, 1)	12
308	26	0.1214360E-01	(1, 2, 2, 7)	12	974	53	0.1613584E-01	(4, 6, 0, 2)	12
328	27	0.1387186E+00	(1, 3, 0, 4)	8	1009	54	-0.2007129E-01	(4, 7, 0, 1)	12

TABLE STIII. Dominant coefficients, $c(I)$, in the CI expansion of the relative LLL ground state (with $\langle L\rangle = 7.330$) in the ($S = 0$, $S_z = 0$) spin sector corresponding to the symmetry-broken state whose single-particle density portrayed in Figs. 5(e,f) of the main text. The CI expansion consists of $I_{\rm total} = 1296$ basis determinants. The index J is introduced to relabel the dominant coefficients, with the dominance criterion being $|c(I)| > 0.001$. 20 determinants with total angular momenta $L = 4$ or 8 participate in this TABLE. Note that $\sum_{i=1}^{20} |c(J)|^2 = 0.9999939$, i.e., the corresponding contribution to the normalization constant differs from unity only in the sixth decimal point.

I	J	$c(J)$	$(l_1\uparrow, l_2\uparrow, l_3\downarrow, l_4\downarrow)$	$\sum_{i=1}^{4} l_i$	I	J	$c(J)$	$(l_1\uparrow, l_2\uparrow, l_3\downarrow, l_4\downarrow)$	$\sum_{i=1}^{4} l_i$
3	1	0.1255794E+00	(0, 1, 0, 3)	4	299	11	0.2212714E+00	(1, 2, 1, 4)	8
9	2	0.1729051E+00	(0, 1, 1, 2)	4	304	12	0.1564648E+00	(1, 2, 2, 3)	8
22	3	0.2555221E+00	(0, 1, 3, 4)	8	328	13	-0.1277153E+00	(1, 3, 0, 4)	8
38	4	-0.2760651E+00	(0, 2, 0, 2)	4	334	14	-0.3832525E+00	(1, 3, 1, 3)	8
53	5	-0.3130074E+00	(0, 2, 2, 4)	8	363	15	0.1278069E+00	(1, 4, 0, 3)	8
73	6	0.1255794E+00	(0, 3, 0, 1)	4	369	16	0.2212714E+00	(1, 4, 1, 2)	8
83	7	0.1278069E+00	(0, 3, 1, 4)	8	543	17	0.2709799E+00	(2, 3, 0, 3)	8
88	8	0.2709799E+00	(0, 3, 2, 3)	8	549	18	0.1564648E+00	(2, 3, 1, 2)	8
118	9	-0.1277153E+00	(0, 4, 1, 3)	8	578	19	-0.3130074E+00	(2, 4, 0, 2)	8
289	10	0.1729051E+00	(1, 2, 0, 1)	4	757	20	0.2555221E+00	(3, 4, 0, 1)	8

TABLE STIV. Dominant coefficients, $c(I)$, in the CI expansion of the relative LLL ground state (with $\langle L\rangle = 8.00002$) in the ($S = 0$, $S_z = 0$) spin sector corresponding to the symmetry-broken state whose single-particle density portrayed in Figs. 5(g,h) of the main text. The CI expansion consists of $I_{\rm total} = 1296$ basis determinants. The index J is introduced to relabel the dominant coefficients, with the dominance criterion being $|c(I)| > 0.001$. 16 determinants (15 with total angular momentum $L = 8$ and 1 with $L = 4$) participate in this TABLE. Note that $\sum_{i=1}^{16} |c(J)|^2 = 0.999989$, i.e., the corresponding contribution to the normalization constant differs from unity only in the fifth decimal point. The coefficient of the determinant with $L = 4$ in the TABLE is two orders (in absolute magnitude) smaller than the coefficients of the 15 determinants with $L = 8$.

I	J	$c(J)$	$(l_1\uparrow, l_2\uparrow, l_3\downarrow, l_4\downarrow)$	$\sum_{i=1}^{4} l_i$	I	J	$c(J)$	$(l_1\uparrow, l_2\uparrow, l_3\downarrow, l_4\downarrow)$	$\sum_{i=1}^{4} l_i$
22	1	-0.2800321E+00	(0, 1, 3, 4)	8	328	9	0.1400277E+00	(1, 3, 0, 4)	8
38	2	0.1260197E-02	(0, 2, 0, 2)	4	334	10	0.4200807E+00	(1, 3, 1, 3)	8
53	3	0.3429776E+00	(0, 2, 2, 4)	8	363	11	-0.1400264E+00	(1, 4, 0, 3)	8
83	4	-0.1400283E+00	(0, 3, 1, 4)	8	369	12	-0.2425468E+00	(1, 4, 1, 2)	8
88	5	-0.2970250E+00	(0, 3, 2, 3)	8	543	13	-0.2970589E+00	(2, 3, 0, 3)	8
118	6	0.1400259E+00	(0, 4, 1, 3)	8	549	14	-0.1714872E+00	(2, 3, 1, 2)	8
299	7	-0.2425213E+00	(1, 2, 1, 4)	8	578	15	0.3430137E+00	(2, 4, 0, 2)	8
304	8	-0.1715068E+00	(1, 2, 2, 3)	8	757	16	-0.2800782E+00	(3, 4, 0, 1)	8

```
(* SUPPLEMENTAL MATERIAL II *)
(* TITLE: "Fractional-quantum-Hall physics and higher-order
momentum correlations
   in few spinful fermionic contact-interacting ultracold atoms
in rotating traps" *)
(* AUTHORS: Constantine Yannouleas and Uzi Landman *)

(* Coder: Constantine Yannouleas, Atlanta, Georgia, USA, 10aug20
*)



(* ---------------------------------- *)
(* Scripts related to N=4 LLL fermions *)
(* For N=6, see another note below *)
(* ---------------------------------- *)

(* Analytic expressions for the F_i(z_1,z_2,z_3,z_4) and
\tilde{F}_i of Sec. IV D *)

ClearAll["Global`*"];

(* Definition of zeta_i, Eq. (22) *)

zeta[1]=a[1]*a[2]*b[3]*b[4];
zeta[2]=a[1]*a[3]*b[2]*b[4];
zeta[3]=a[1]*a[4]*b[2]*b[3];
zeta[4]=a[2]*a[3]*b[1]*b[4];
zeta[5]=a[2]*a[4]*b[1]*b[3];
zeta[6]=a[3]*a[4]*b[1]*b[2];

(* Define matrices entering in LLL basis determinants; the
1/Sqrt[N!] normalization is omitted
in the Slater determinants here *)

mat[l1_,l2_,l3_,l4_]:=
 {{z1^l1*a[1]/Sqrt[Pi*l1!], z2^l1*a[2]/Sqrt[Pi*l1!],
z3^l1*a[3]/Sqrt[Pi*l1!], z4^l1*a[4]/Sqrt[Pi*l1!]},
```

```
  {z1^l2*a[1]/Sqrt[Pi*l2!], z2^l2*a[2]/Sqrt[Pi*l2!],
z3^l2*a[3]/Sqrt[Pi*l2!], z4^l2*a[4]/Sqrt[Pi*l2!]},
  {z1^l3*b[1]/Sqrt[Pi*l3!], z2^l3*b[2]/Sqrt[Pi*l3!],
z3^l3*b[3]/Sqrt[Pi*l3!], z4^l3*b[4]/Sqrt[Pi*l3!]},
  {z1^l4*b[1]/Sqrt[Pi*l4!], z2^l4*b[2]/Sqrt[Pi*l4!],
z3^l4*b[3]/Sqrt[Pi*l4!], z4^l4*b[4]/Sqrt[Pi*l4!]}};

(* The coefficients in Eq. (32); the index 8 indicates the L=8
total angular momentum *)

c8[1]=c1; c8[16]=c1; c8[4]=c1/2;
c8[6]=-c1/2; c8[9]=-c1/2; c8[11]=c1/2;
c8[3]=c2; c8[15]=c2;
c8[8]=-c2/2; c8[14]=-c2/2;
c8[5]=c3; c8[13]=c3;
c8[7]=c4; c8[12]=c4;
c8[10]=c5;

(* The corresponding CI wave function [Eq. (9)] using the 15
determinants in TABLE STIV
   in SUPPLENENTAL MATERIAL I   *)

ciwfL8=c8[1]*Det[mat[0,1,3,4]]+
   c8[3]*Det[mat[0,2,2,4]]+
   c8[4]*Det[mat[0,3,1,4]]+
   c8[5]*Det[mat[0,3,2,3]]+
   c8[6]*Det[mat[0,4,1,3]]+
   c8[7]*Det[mat[1,2,1,4]]+
   c8[8]*Det[mat[1,2,2,3]]+
   c8[9]*Det[mat[1,3,0,4]]+
   c8[10]*Det[mat[1,3,1,3]]+
   c8[11]*Det[mat[1,4,0,3]]+
   c8[12]*Det[mat[1,4,1,2]]+
   c8[13]*Det[mat[2,3,0,3]]+
   c8[14]*Det[mat[2,3,1,2]]+
   c8[15]*Det[mat[2,4,0,2]]+
   c8[16]*Det[mat[3,4,0,1]];

(* The F_i functions associated with ciwf8; see Eq. (39) *)
```

```
F[i_]:=Coefficient[ciwfL8,zeta[i]];

(* The tilded F_i functions of Eqs. (40)-(45), denoted here as
FF[i] *)

FF[1]=(F[1]+F[3]+F[4]+F[6]-2*F[2]-2*F[5])/Sqrt[12];

FF[2]=(F[1]-F[3]-F[4]+F[6])/2;

FF[3]=(F[6]-F[1])/Sqrt[2];

FF[4]=(F[5]-F[2])/Sqrt[2];

FF[5]=(F[4]-F[3])/Sqrt[2];

FF[6]=(F[1]+F[2]+F[3]+F[4]+F[5]+F[6])/Sqrt[6];

(*********************

(* After importing the file into a MATHEMATICA notebook, copy and
paste the following commands *)

(* Show that the following are vanishing *)

FF[3]//FullSimplify

FF[4]//FullSimplify

FF[5]//FullSimplify

FF[6]//FullSimplify


(* Derive Eq. (47) *)

(* Set the z_i's at the corners of a square *)

z1=z0; z2=z0*I; z3=-z0; z4=-z0*I;
```

```
FF[1]

FF[2]//Factor

Clear[z1,z2,z3,z4]

*******************)

(* Derive Eq. (50) in Sec. V B *)

(* The CI wave function [lhs of Eq. (50)] using the 6
determinants in TABLE I *)

ciwfL6S2Sz0=(-Det[mat[0,1,2,3]]+Det[mat[0,2,1,3]]-Det[mat[0,3,1,2
]]-

Det[mat[1,2,0,3]]+Det[mat[1,3,0,2]]-Det[mat[2,3,0,1]])/Sqrt[6];

(******************
(* After importing the file into a MATHEMATICA notebook, copy and
paste the following *)

Clear[z1,z2,z3,z4]; ciwfL6S2Sz0//Factor

*******************)

(* Derive Eq. (51) in Sec. VI A *)

mat2[l1_,l2_,l3_,l4_]:=
 {{z1^l1*a[1]/Sqrt[Pi*l1!], z2^l1*a[2]/Sqrt[Pi*l1!],
z3^l1*a[3]/Sqrt[Pi*l1!], z4^l1*a[4]/Sqrt[Pi*l1!]},
  {z1^l2*a[1]/Sqrt[Pi*l2!], z2^l2*a[2]/Sqrt[Pi*l2!],
z3^l2*a[3]/Sqrt[Pi*l2!], z4^l2*a[4]/Sqrt[Pi*l2!]},
  {z1^l3*a[1]/Sqrt[Pi*l3!], z2^l3*a[2]/Sqrt[Pi*l3!],
z3^l3*a[3]/Sqrt[Pi*l3!], z4^l3*a[4]/Sqrt[Pi*l3!]},
  {z1^l4*a[1]/Sqrt[Pi*l4!], z2^l4*a[2]/Sqrt[Pi*l4!],
z3^l4*a[3]/Sqrt[Pi*l4!], z4^l4*a[4]/Sqrt[Pi*l4!]}};
```

```
ciwfL6S2Sz2=Det[mat2[0,1,2,3]];

(******************
(* After importing the file into a MATHEMATICA notebook, copy and
paste the following *)

Clear[z1,z2,z3,z4]; ciwfL6S2Sz2//Factor

*******************)

(* ---------------------------------- *)
(* Scripts related to N=6 LLL fermions *)
(* ---------------------------------- *)

(* Definition of Zeta_i, Eq. (B1) in Appendix B, denoted as ZZ
here *)

list3a=Subsets[Table[i,{i,1,6}],{3}];
list6 = Table[i, {i, 1, 6}];
list3b = Table[list6 /. {list3a[[jj, 1]] -> Nothing, list3a[[jj,
2]] -> Nothing,
    list3a[[jj, 3]] -> Nothing}, {jj, 1, Length@list3a}];
Do[ZZ[ii] = a[list3a[[ii, 1]]]*a[list3a[[ii, 2]]]*a[list3a[[ii,
3]]]*
   b[list3b[[ii, 1]]]*b[list3b[[ii, 2]]]*b[list3b[[ii, 3]]], {ii,
1, Length@list3a}];

(* Define matrices for N=6 entering in LLL basis determinants;
the 1/Sqrt[N!]
normalization is omitted in the Slater determinants here, along
with the factor
1/(Pi^3*Sqrt[l1!l2!l3!l4!l5!l6!]); for the single-particle
angular momenta in TABLE II,
this yields a common factor for all 20 dominant Slater
determinants *)

mat6[l1_, l2_, l3_, l4_, l5_, l6_] :=
    {{z1^l1*a[1], z2^l1*a[2], z3^l1*a[3], z4^l1*a[4], z5^l1*a[5],
z6^l1*a[6]},
```

```
     {z1^l2*a[1], z2^l2*a[2], z3^l2*a[3], z4^l2*a[4], z5^l2*a[5],
z6^l2*a[6]},
     {z1^l3*a[1], z2^l3*a[2], z3^l3*a[3], z4^l3*a[4], z5^l3*a[5],
z6^l3*a[6]},
     {z1^l4*b[1], z2^l4*b[2], z3^l4*b[3], z4^l4*b[4], z5^l4*b[5],
z6^l4*b[6]},
     {z1^l5*b[1], z2^l5*b[2], z3^l5*b[3], z4^l5*b[4], z5^l5*b[5],
z6^l5*b[6]},
     {z1^l6*b[1], z2^l6*b[2], z3^l6*b[3], z4^l6*b[4], z5^l6*b[5],
z6^l6*b[6]}};

(* Derive Eq. (52) in Sec. VI B *)

(* The CI wave function [lhs of Eq. (52)] using the 20
determinants in TABLE II
and taking into consideration the sign of the c(J) coefficients
*)

wfnp6 = -Det[mat6[0, 1, 2, 3, 4, 5]] + Det[mat6[0, 1, 3, 2, 4,
5]] -
  Det[mat6[0, 1, 4, 2, 3, 5]] + Det[mat6[0, 1, 5, 2, 3, 4]] -
  Det[mat6[0, 2, 3, 1, 4, 5]] + Det[mat6[0, 2, 4, 1, 3, 5]] -
  Det[mat6[0, 2, 5, 1, 3, 4]] - Det[mat6[0, 3, 4, 1, 2, 5]] +
  Det[mat6[0, 3, 5, 1, 2, 4]] - Det[mat6[0, 4, 5, 1, 2, 3]] +
  Det[mat6[1, 2, 3, 0, 4, 5]] - Det[mat6[1, 2, 4, 0, 3, 5]] +
  Det[mat6[1, 2, 5, 0, 3, 4]] + Det[mat6[1, 3, 4, 0, 2, 5]] -
  Det[mat6[1, 3, 5, 0, 2, 4]] + Det[mat6[1, 4, 5, 0, 2, 3]] -
  Det[mat6[2, 3, 4, 0, 1, 5]] + Det[mat6[2, 3, 5, 0, 1, 4]] -
  Det[mat6[2, 4, 5, 0, 1, 3]] + Det[mat6[3, 4, 5, 0, 1, 2]];

(* Show that wfnp6 is proportional to a Vandermonde determinant
for N=6 LLL fermions *)

(* sumZeta/Sqrt[6] below is the spin eigenfunction for N=6
fermions with S=3, S_z=0 *)

sumZeta = Sum[ZZ[i], {i, 1, 20}];

(******************
```

```
(* After importing the file into a MATHEMATICA notebook, copy and paste the following *)

(wfnp6//Expand//FullSimplify)/sumZeta//FullSimplify

**********)
```